Design and Development of an Airborne Microwave Radiometer for Atmospheric Sensing

by

Michael P. Scarito

S.B. EECS, M.I.T. (2010)
S.B. Physics, M.I.T. (2010)

Submitted to the Department of Electrical Engineering and Computer Science
in partial fulfillment of the requirements for the degree of

Master of Engineering in Electrical Engineering and Computer Science

at the

MASSACHUSETTS INSTITUTE OF TECHNOLOGY

June 2011

Author .....
Department of Electrical Engineering and Computer Science
May 20, 2011

Certified by .....
William J. Blackwell
Senior Staff, MIT Lincoln Laboratory
Thesis Supervisor

Certified by .....
David H. Staelin
Professor of Electrical Engineering
Thesis Supervisor

Accepted by .....
Christopher J. Terman
Chairman, Department Committee on Graduate Theses

This work is sponsored by the National Oceanic and Atmospheric Administration under Air Force Contract #FA8721-05-C-0002. Opinions, interpretations, conclusions, and recommendations are those of the author and are not necessarily endorsed by the United States Government.

Design and Development of an Airborne Microwave Radiometer for Atmospheric Sensing

by

Michael P. Scarito

Submitted to the Department of Electrical Engineering and Computer Science
on May 20, 2011, in partial fulfillment of the
requirements for the degree of
Master of Engineering in Electrical Engineering and Computer Science

Abstract

Satellite-based passive microwave remote sensing is a valuable tool for global weather monitoring and prediction. This thesis presents the design and development of a low-cost airborne weather sensing instrument to independently validate a satellite-based sensor platform. The NPOESS Aircraft Sounder Testbed - K-band (NAST-K) is a passive microwave radiometer operating over approximately 200 MHz bandwidth centered at 23.8 GHz and 31.4 GHz, whose data can be used to find surface water, humidity, and temperature conditions. NAST-K flies along with the existing NAST-M instrument at an altitude of 18 km in the NASA ER-2 high altitude aircraft. The primary function of NAST-K is to provide coverage of channels 1 and 2 of the Advanced Technology Microwave Sounder (ATMS) aboard the NPOESS Preparatory Project (NPP) satellite, scheduled to be launched in October 2011. The combined NAST-M/K system can validate the performance of ATMS on all channels with data products up to 17 km, by underflying the satellite along the same ground track and collecting correlated data. NAST-K has full-width at half maximum beamwidths of 7.4° and 6.8° for the two channels respectively, which is approximately consistent with NAST-M. The effective spot size of NAST-K is 2.3 km in diameter for the wider 23.8 GHz channel at nadir, providing an areal resolution approximately 1000 times greater than ATMS. The major contributions of this thesis include the system-level design of NAST-K, the development of the video amplifier and embedded environmental monitor, and the analysis of the antenna system.

Thesis Supervisor: William J. Blackwell
Title: Senior Staff, MIT Lincoln Laboratory

Thesis Supervisor: David H. Staelin
Title: Professor of Electrical Engineering

Acknowledgments

I would like to thank Bill Blackwell for his guidance throughout the development of this project. Bill made himself very accessible despite his busy schedule, and he provided important encouragement to help me push forward in the project. In addition, I want to recognize Vince Leslie for serving as an informal second mentor on this project. Together, they were both tremendously useful in providing a weather science perspective for the work, as well as important lessons learned in the development of an airborne instrument from their past work on NAST-M.

Prof. Dave Staelin was an excellent technical resource. His extensive knowledge about practical radiometer design was very informative when determining project requirements. Prof. Jose Martinez of Northeastern University helped substantially with the initial antenna design and provided significant guidance as I made refinements to the design later on.

I worked with many staff members at M.I.T. Lincoln Laboratory to develop this project, and they were all very helpful. Idahosa Osaretin, Mike DiLiberto, Dave Kusinsky, and Joe Costa all contributed advice on the system design. Allan Nichols, Larry Retherford and Bob Bucknam provided a lot of support on the mechanical side. They took my rough models and produced designs that we could actually build. Larry helped in a big way by taking measurements of the actual aircraft in Edwards, CA, since our drawings were incomplete. One person who really went out of his way to help was Jeff Shultz. On several occasions he took time out of his schedule to go over my circuit designs with me and point out any potential issues, even though NAST-K was not his project.

Contents

List of Figures

List of Tables

Chapter 1

Introduction

Satellite-based remote sensing is one of the primary data sources for atmospheric weather measurement, modelling, and forecasting. Compared with the alternative of direct observation tools such as ground stations, weather balloons, or rocketsondes, which only provide localized points of data, remote sensing provides global coverage at high resolution updated multiple times daily. The tradeoff is that instead of directly measuring parameters such as temperature, barometric pressure, humidity, and wind speed and direction, these parameters must be inferred by the manner in which the atmosphere absorbs, transmits, or reflects electromagnetic radiation in the microwave, infrared, visible, and ultraviolet regions.

The current operational weather satellite system of the National Oceanic and Atmospheric Administration (NOAA) is the Polar Operational Environmental Satellite (POES) system. This system provides global coverage four times per day, and includes several passive remote sensing instruments for weather observation. The POES payloads include two microwave sounders: the Advanced Microwave Sounding Unit (AMSU), and additionally the Microwave Humidity Sounder (MHS) on newer satellites. These instruments are primarily intended to measure atmospheric humidity with respect to altitude, as well as water content in clouds[15]. Microwave sensors have lower spatial resolution than their infrared or visible counterparts, but they have the distinct advantage of being able to operate through cloud obscuration, which is likely when the weather data is the most valuable. The next generation platform for NOAA is the National Polar-orbiting Operational Environmental Satellite System (NPOESS). The first satellite in this system, the

NPOESS Preparatory Project (NPP), is currently scheduled to be launched in October 2011. The satellite will contain a new microwave radiometer, the Advanced Technology Microwave Sounder (ATMS), which is the next generation replacement for AMSU-A.

The primary work pertaining to this thesis, the NPOESS Atmospheric Sounder Testbed - K-band (NAST-K), is a new passive microwave radiometer design measuring two channels near 23.8 GHz (K-band) and 31.4 GHz (Ka-band). These channels are primarily used together to estimate cloud liquid water, integrated water vapor, and surface temperature. Radiance observations in the K-band region are more strongly attenuated due to water vapor than those in the Ka-band, and the relatively unattenuated K-band signal can be fit with the expected emissivity of the Earth's surface at its surface temperature [18]. The principal function of NAST-K is to validate the two corresponding channels on ATMS. When flown along with the heritage instrument NAST-M, the pair provides coverage of most of the channels on ATMS with independently designed receivers. In the mission plan, NAST-M and NAST-K will fly on a high-altitude aircraft directly below the ground track of the satellite. When the satellite passes overhead, the two airborne instruments will be collecting data which is both temporally and geographically coincident with the satellite data. As NAST-M/K can be extensively calibrated before and after the satellite under-flight, the two data sets can be compared against each other in order to demonstrate proper performance of ATMS.

The original plan called for NAST-K to be an upgrade of the NAST-M instrument, but the decision was soon made to create NAST-K as a separate instrument due the lack of space to add hardware to the NAST-M payload. This provides the advantage of having two separate independently-operating instruments available, where the failure of one will not affect the other, and where the two instruments can be deployed individually.

NAST-K operates as a cross-track scanner, collecting data in a swath to the left and right of the aircraft as it flies forward. This design is consistent with that of NAST-M, which will allow NAST-M and NAST-K to operate in a synchronized configuration. NAST-M and NAST-K have very similar antenna beamwidths which will allow them to collect easily correlated data from the same paths through the atmosphere. NAST-K does provide several changes over the NAST-M design which are optimized for the lower frequency of operation. These include a direct-detect radiometer front end which provides a reduced noise figure over a superheterodyne design at the cost of more challenging RF

bandpass filters, a single radiometer feed for both frequency bands, an offset parabolic reflector to provide a tighter pencil-beam, and new voltage and temperature monitoring instrumentation.

NAST-K will be initially deployed along side NAST-M in the NASA ER-2 high altitude aircraft. Both NAST-M and NAST-K are mounted in the rear of the ER-2 wing pod, with support electronics in the middle of the pod. NAST-K views the earth through a hole cut in the bottom of the pod, allowing the instrument to look from side to side. The pod will have an additional hole cut in the top allowing the instrument to look up into space as a calibration reference. NAST-M has demonstrated the validity of airborne measurement for satellite microwave radiometer calibration through its performance on several flight campaigns. The addition of NAST-K will expand its capability to provide temperature and humidity sensing from the surface up through an altitude of 17 km.

I have supported the design of most aspects of the NAST-K system. I have produced two original printed circuit board designs: the video amplifier which amplifies and buffers the output of the radiometer front end in order to pass it to the analog-to-digital converter, and the embedded environmental monitor which measures temperatures and supply voltages across the system, particularly around the radiometer front end. I have designed a parabolic horn and reflector model to evaluate the performance of the design, and designed a preliminary parabolic reflector for manufacturability. Furthermore, I have developed an initial parabolic reflector solid model for manufacturability. For the radiometer system, I determined the required performance parameters to provide compatibility with ATMS. I specified and sourced many of the parts in the system, including the scan drive motor, the flight computer system and enclosure, and the camera system and support electronics. I set up the initial software platform for development on the NAST-K flight computer, and set up the hardware peripherals on the flight computer. For the embedded environmental monitor, which was intended to be shared between NAST-K and the MicroMAS project, I worked with the MicroMAS team to determine requirements and help specify the interfaces for the system.

Chapter 2

Background

2.1 Microwave Radiometry

Microwave radiometry is simply the passive measurement of power incident on an antenna at a given frequency. In remote sensing applications, the antenna is typically highly directional, receiving energy from a localized area. The physical parameter being measured is the thermal radiation from the earth or from space and how much this radiation is reflected or absorbed by the Earth's surface or by matter in the atmosphere. Since we are intending to measure thermal energy, the received power levels are extremely low. For some perspective, when discussing a normal radio receiver a typical figure of merit is the signal-to-noise ratio. In our case, the parameter of interest is exactly that thermal noise, which we must sense with enough power to detect minute changes. To make matters worse, unlike a traditional receiver we cannot do anything to correlate our signal and increase the effective signal-to-noise ratio, since we are measuring a random process. This means that any noise introduced anywhere in the receiver system will decrease the effective sensitivity of the system, because it will impose a lower limit on the change in power that we can detect in any finite time interval [7].

2.1.1 Antenna Gain

When our radiometer is observing an environment, it does so through the use of an antenna. This antenna has a variable gain with respect to both frequency and look angle of $G_a(\theta, \phi, \nu)$. Our receiver has a certain bandwidth for a given channel, and we would

like our antenna gain to be flat across this region. It should be noted that in some cases a variable antenna gain over frequency can be calibrated for, but it can present certain issues as we will see in Section 2.4.2. Antennas are passive elements, meaning the integral of the gain per solid angle over the entire far field sphere around the antenna is equal to that of an isotropic antenna, minus any losses. Thus, when an antenna has gain above unity in one region, it has corresponding gain below unity in other regions. For a microwave radiometer, this is an interesting result, because neglecting losses in the antenna, a received power level will correspond to a specific average incident power density (power per solid angle) weighted over the antenna beam, and this power density to received power relationship is independent of the specifics of the antenna used. As the beam pattern of the antenna changes, only the weighting for the average will change, so if lossless antennas with different beam patterns are viewing different-sized scenes with the same power density, their power output will be identical to each other [25].

2.1.2 Receiver gain

Measurements made by a microwave radiometer are sampled as an analog voltage, which is a rectified and low-pass filtered measurement of the signal within the RF pass-band of the system. This voltage is proportional to the received power. If we denote the power per unit frequency exiting the feed port of the antenna $\Phi_a(\nu, t)$ and the gain of the receiver $G_r(\nu)$, then the signal level at the detector will be $\Phi_d(\nu, t) = \Phi_a(\nu, t)G_r(\nu)$. The detector has a response proportional to its input power. If we denote the detector response as $G_d(\nu)$, and assume some additional gain G_v for the system following rectification (which does not have a frequency dependence because it comes after rectification), we have the instantaneous output voltage

$$V_o(t) = G_v \int_0^\infty G_d(\nu)G_r(\nu)\Phi_a(\nu, t)\, d\nu. \tag{2.1}$$

This voltage is typically low-pass filtered, so as to appear as $V_o(t)$ convolved with the tail of an exponential function with unity area. To simplify this model, we assume that the receiver gain is zero outside of some passband, and further that the response of the detector is flat within that passband. If our receiver is centered at some $\nu = \nu_c$ with

passband width $\Delta\nu$, the output voltage is then

$$V_o(t) = G_v \int_{\nu_c-\Delta\nu/2}^{\nu_c+\Delta\nu/2} G_d G_r(\nu) \Phi_a(\nu, t)\, d\nu. \tag{2.2}$$

Since we are eventually interested in finding an average power level P_a in the passband, rather than a power per unit frequency, we can simplify the model further to assume a power level and receiver response that do not vary with frequency. In this case we assume that $P_a \approx \Phi(\nu)\Delta\nu$. This then simplifies the signal to

$$V_o(t) = G_v G_d G_r P_a(t). \tag{2.3}$$

We can then solve for the input power required to produce a given output voltage as

$$P_a(t) = \frac{V_o(t)}{G_d G_r G_v}. \tag{2.4}$$

In practice, the constant of proportionality is found through the periodic calibration process (see Section 2.4.2) so we are primarily concerned with the linear relationship between P_a and V_o. Since the white calibration signals pass through the receiver and detector, as long as we assume a white signal over the pass band from the measured signal, the assumptions made about the receiver and detector gain response over frequency are actually unnecessary.

2.1.3 Noise equivalent delta-temperature

A performance parameter for microwave radiometer sensitivity is the root-mean-square (RMS) noise equivalent delta-temperature, or ΔT_{rms}. This figure gives the error associated with a given brightness temperature measurement. The noise equivalent temperature is based on the integration time, the receiver bandwidth, and the noise temperatures of the receiver and the environment. First, the receiver temperature is found as

$$T_r = (10^{\frac{NF}{10}} - 1)T_a \tag{2.5}$$

where NF is the receiver noise figure and T_a is the ambient noise temperature. The noise equivalent delta-temperature is then

$$\Delta T_{rms} = \frac{T_a + T_r}{\sqrt{\tau \Delta \nu}} \tag{2.6}$$

where τ is the integration time and $\Delta \nu$ is the bandwidth [25].

2.2 Radiative Transfer

A radiometer designed for weather sensing is intended to receive radiation incident on the Earth from space, or radiating from the Earth's surface or the atmosphere. Before this radiation reaches the radiometer antenna and can be measured it can be absorbed or reflected by the Earth's surface or by matter in the atmosphere. If we are searching for something that is primarily radiative at a certain frequency, then a higher signal indicates more of that thing. On the other hand, if we are searching for something that attenuates at a certain frequency, we are looking for a lower signal. We typically require some sort of baseline, so an example measurement might compare signals at two frequencies: one which is strongly attenuated by the matter of interest, and another which is negligibly attenuated. Finally, we may be interested in something which is reflective at a certain frequency, in which case a higher signal would indicate a weaker feature for an airborne or satellite-borne sensor, whereas a higher signal would indicate a stronger feature for a ground-based sensor.

It is important to remember that in interpreting data from any remote sensing system, we must determine not only the value and distribution of some physical parameter but also the very nature of the scene being viewed. There are multiple phenomena which could produce the same response in a given measurement. As an example, when viewing the surface over the earth, over land we would view much more intense radiation in the microwave band than over water. This is due to the fact that water is highly reflective at microwave frequencies compared to land, and the radiation being reflected is primarily incident from the cosmic microwave background of outer space. The reduced signal could also be due to strong attenuation of radiation from land by clouds. To interpret any measurement of a remote sensing system, the data is frequently combined with a

host of different measurements in order to disambiguate the complicated interactions in atmospheric physics.

2.2.1 Atmospheric Absorption

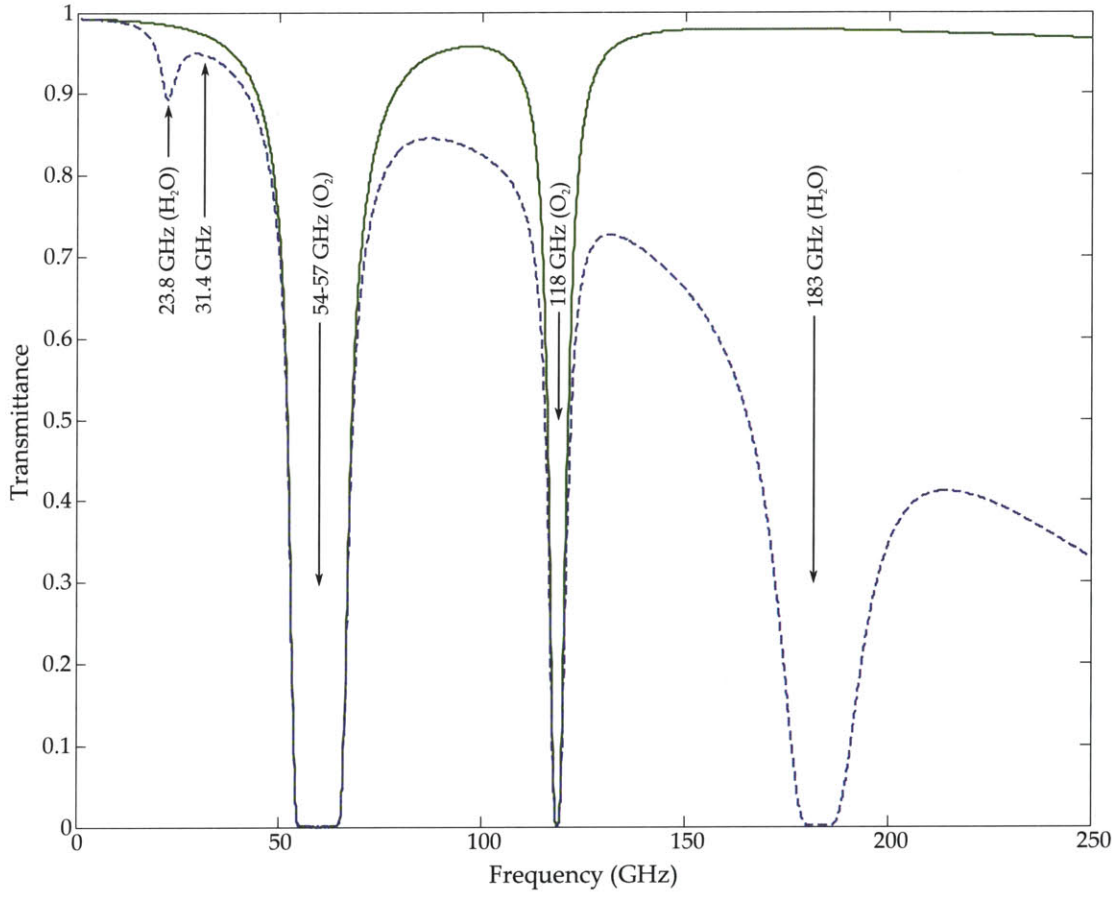

Figure 2-1: Atmospheric transmittance in the microwave band, based on the 1976 Standard Atmosphere[17]. The transmittance corresponds to viewing a non-reflective surface from space looking at nadir. The solid green line is the transmittance with no atmospheric water vapor, and the dashed blue line is the transmittance with water vapor from the 1976 standard included. Several relevant frequency bands for oxygen and water vapor sensing are shown. The data is generated using the radiative transfer software from Rosenkranz[20].

Any radiation sensed by a high altitude radiometer will be measuring a combination of the radiated energy from the atmosphere and the radiated energy from the Earth's surface. Depending on the altitude at which the energy is radiated, the energy will be attenuated by the atmosphere by a varying magnitude. A typical transmittance for en-

ergy radiated by the Earth's surface is shown in Figure 2-1. This plot shows the strong water vapor absorption bands at 23.8 GHz and 183 GHz, and gives an idea of how the two channels at 23.8 GHz and 31.4 GHz can be compared to determine atmospheric water content. These absorption bands behave differently depending on pressure, where at a lower pressure an absorption band will be narrower and at a higher pressure the absorption band will broaden. This allows a radiometer with a series of channels spaced out around the center of an absorption band to measure phenomena at varying altitudes. This technique is described in [2] and is the reason why many radiometers have a bank of double-sideband channels centered about some frequency.

2.2.2 Brightness Temperature

Rather than antenna power, most atmospheric science models will use the equivalent brightness temperature when interpreting data from microwave radiometers. Brightness temperature, or T_b, is the temperature of a black body which would produce the same power as a given measurement. A black body is an idealized physical object which absorbs all incident radiation and radiates entirely incandescently. The intensity of this incandescent radiation is described by Planck's law. We can use Planck's law to find the time-averaged power density per unit frequency, per unit solid angle, at a given frequency, for a black body at a given temperature by the relationship

$$B_\nu(T) = \frac{2h\nu^3}{c^2}\frac{1}{e^{\frac{h\nu}{kT}} - 1} \tag{2.7}$$

where $h \approx 6.626 \times 10^{-34}\,\mathrm{m^2\,kg\,s^{-1}}$ is Planck's constant and $k \approx 1.381 \times 10^{-23}\,\mathrm{m^2\,kg\,s^{-2}\,K^{-1}}$ is the Boltzmann constant. This appears to be a very nonlinear relationship with temperature, but we can make a simplification. Since our frequency is very low compared to temperature, or more specifically $h\nu \ll kT$ by two orders of magnitude at $T = 300\,\mathrm{K}$ and $\nu = 31.4\,\mathrm{GHz}$, we can instead use the simpler Rayleigh-Jeans law, which gives us

$$B_\nu(T) \approx \frac{2\nu^2 k}{c^2}T, \tag{2.8}$$

or rewriting for temperature,

$$T_B(\nu) = \left(\frac{c^2}{2\nu^2 k}\right)B_\nu. \tag{2.9}$$

[25] Since we have no information about how the power varies over our passband, only a total power, we must simplify the law by assuming a constant $T_B(\nu)/B_\nu$ across the passband. This allows us to define P_a in terms of a single B_ν as

$$P_a = \int_{\nu_c - \Delta\nu/2}^{\nu_c + \Delta\nu/2} B(\nu)\, d\nu \approx B_\nu \Delta\nu. \tag{2.10}$$

This holds so long as $\Delta\nu \ll \nu$. The modified Rayleigh-Jeans relationship is now

$$T_B(\nu) = \left(\frac{c^2}{2\nu^2 \Delta\nu k}\right) P_a. \tag{2.11}$$

This is a convenient linear relationship between received power and brightness temperature.

2.3 Atmospheric Science in K- and Ka-bands

The 23.8 GHz and 31.4 GHz channels in AMSU, ATMS, and NAST-K are commonly used to measure surface brightness temperatures and atmospheric water content. There are several algorithms provided by NESDIS for retrieving physical parameters from brightness temperatures recorded at these frequencies [18]. For data collected over the ocean, these two channels can be used to calculate cloud liquid water and water vapor in the vertical column viewed by the instrument. On land, snow cover can be characterized using the brightness temperature difference between the two channels. Snow water equivalent, which is a parameter describing the equivalent depth of pure water in a region of snow cover, can be estimated as well. Using one of the channels from NAST-M, at 50.3 GHz, in conjunction with the two NAST-K channels we can find sea ice concentration as a percentage of the surface area covered by the measurement spot. We can also estimate land surface temperature and surface emissivity at these three frequencies using their brightness temperatures [18].

2.4 Receiver Calibration

Calibration is an important part of any instrumentation system. In the case of a microwave radiometer, gain calibration is critical because the receiver gain can vary greatly

with instrument temperature and supply voltage. Certain calibration tasks can be performed while the instrument is in the lab, termed ground calibration. Other tasks must be performed while the instrument is running to help determine parameters that can change over time or with parameters that are difficult to characterize.

2.4.1 Ground Calibration

Many of the parameters of the system can be measured on the ground to aid in characterizing the system performance. These parameters are measured well before the flight, and thus cannot reflect any drift over time. We can very accurately characterize the system's gain linearity with respect to input brightness temperature by using an external calibration source in view of the feed horn, or by feeding a source directly into the antenna port of the radiometer. By regulating the RFE temperature and supply voltages we can also accurately characterize their effect on system gain across the input range. We can measure the saturation point of the receiver as well as the video amplifier and then configure the gain to prevent saturation during operation.

2.4.2 Operational Calibration

Since the receiver gain is highly dependent on temperature and supply voltage, and it is difficult to fully characterize this dependence on the ground, the gain of the receiver is directly measured periodically. This measurement is performed with the use of both internal and external calibration references. External calibration references are objects of known brightness temperature or radiated power that the antenna is pointed at. Internal references are instead sources that can be fed into the radiometer RF front end, but do not pass through the antenna system.

To characterize receiver gain, a minimum of two reference sources are needed. In Section 2.1.2 we showed that the relationship between power at the antenna port and the output voltage are related by

$$V_o(t) = G_v G_d G_r P_a(t). \tag{2.12}$$

This assumes that there is no DC offset in the diode detector, the video amplifier, or the analog-to-digital converter, so a correction factor of a can be used to compensate for that. Also, we can fold the response factors $G_v\sqrt{G_d G_r}$ into the factor b, so the relationship is

now

$$V_o = a + bP_a. \tag{2.13}$$

If we measure two reference sources, the first with power P_1 and producing output voltage V_1, and the second with power P_2 and corresponding output voltage V_2, we can solve the equations $V_1 = a + b\sqrt{P_1}$ and $V_2 = a + b\sqrt{P_2}$ for a and b. So long as the receiver gain and DC offset do not change between when the calibration is performed and when the measurements are taken, we don't actually need any prior knowledge of the system gain and offset. This calibration is extremely valuable, but is only accurate if performed frequently. The presence of an additional reference source can serve as a cross-check for the proper performance of the other reference sources, and can also be used to perform a least-squares linear regression to find more accurate values of a and b. Furthermore, if the instrument has a non-linear response, perhaps in the form of a large second order term or due to an amplifier reaching saturation at the high end, a third calibration reference can aid in detection. The additional calibration source increases confidence in the correct operation of the instrument.

2.5 Antenna physics

2.5.1 Parabolic reflectors

Parabolic reflectors are conducting surfaces intended to receive a collimated beam and focus it down to a point. This is useful in achieving very narrow pencil beams from broader-beam feed antennas. Parabolic reflectors are typically used at higher frequencies as their diameter must be at least several times larger than the wavelength to be received in order to be useful. At low frequencies below about 30 MHz the reflectors become prohibitively large. At microwave frequencies, parabolic reflectors are perhaps the most common way of obtaining a directional beam [4].

In Cartesian coordinates, a parabolic reflector can be defined by the surface satisfying

$$z = \frac{x^2 + y^2}{4f}. \tag{2.14}$$

This surface has infinite extent over all x and y, and will take any electromagnetic wave propagating in the $-\hat{z}$ direction and focus it at the point $(0, 0, f)$. Since the center of the

surface is at the origin, f is the focal length of the reflector. The vector $\hat{z}$ is known as the boresight of the reflector.

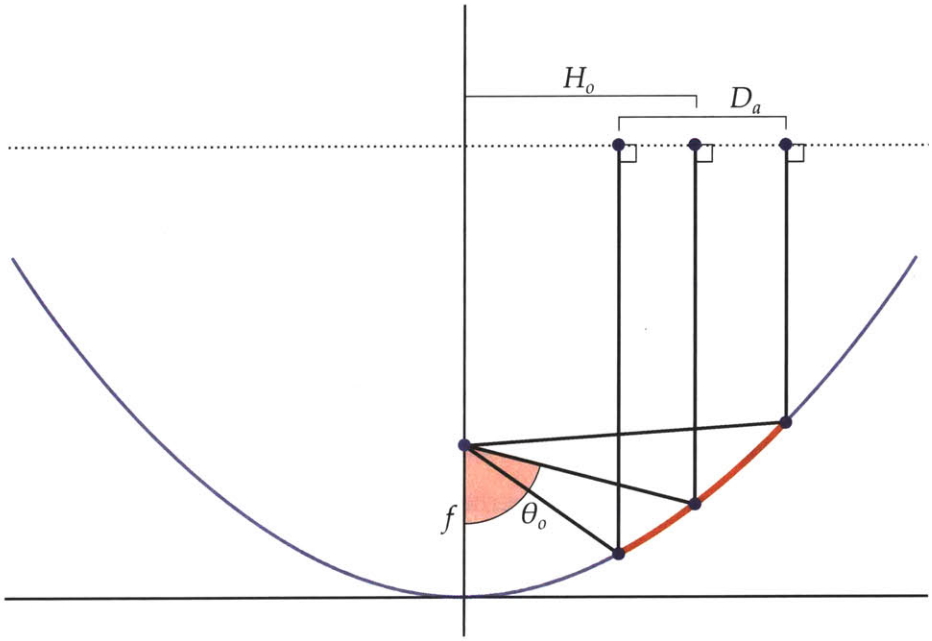

Figure 2-2: Cross-section geometry of an offset parabolic reflector with focal length f. The parabolic reflector covers the dark red portion of the parabola, and has diameter D_a. The boresight is offset by a distance H_o from the centerline of the parabola, and the feed direction is offset by θ_o from the boresight. The paths of idealized incident rays are shown as black lines.

In reality, a parabolic reflector has finite extent with the surface covering some finite region of x and y. The curve defining the edge of this region is known as the rim of the reflector. The rim is usually circular, in which case it could be defined by

$$\frac{D_a^2}{4} = (x - x_0)^2 + (y - y_0)^2. \tag{2.15}$$

where D_a is the diameter of the circular rim. Although an infinite reflector receives only perfectly collimated radiation, a finite reflector instead has a beam which diverges at some angle. This angle is the beamwidth, which is related to the wavelength $\lambda = c/\nu$ and diameter as

$$BW = k_1 \frac{\lambda}{D_a}. \tag{2.16}$$

The parameter k_1 is around 60 or 70, and thus this relationship can only be used to determine an approximate value for the beamwidth [4]. To find a more accurate beamwidth

for a parabolic reflector, numerical physical optics (PO) analysis is typically used. This allows for the analysis of non-elliptical rims, but does not take into account other effects, including diffraction due to the edge of the reflector and due to surface roughness, but provides a fairly accurate model in most cases [23]. The point (x_0, y_0) is the center of the rim. If this point is not at the origin, the reflector is known as an offset parabolic reflector. An offset parabolic reflector can be used to prevent the feed antenna from obscuring the aperture of the reflector and to produce a specific angle between the feed and the boresight. One use of an offset reflector is to design a geometry with a fixed feed and a rotating reflector. This design allows the system to look in different directions without rotating the entire receiver.

Another important parameter in characterizing a parabolic reflector is the ratio between the focal length and aperture diameter, or f/D_a. This parameter allows us to find the half-angle subtended by reflector at the focal point, β, as

$$\cot\beta = 2\frac{f}{D_a} - \frac{1}{8}\frac{D_a}{f}. \tag{2.17}$$

The angle β is used to match the beam of the feed antenna to the parabolic reflector. Any radiation from the feed falling outside β does not interact with the parabolic reflector. This is known as spillover, and a feed with significant spillover is said to over-illuminate the reflector. Over-illumination increases the sidelobe and backlobe levels of the antenna system, and decreases the beam efficiency. On the other hand, a feed which has a half-angle beamwidth significantly smaller than β will under-illuminate the reflector. The primary downside of an under-illuminated reflector is inefficiency in size, weight, and cost, since the region of the reflector not illuminated by the feed provides no benefit to the antenna system.

2.5.2 Horn antennas

A horn antenna is a radiator designed to match a waveguide terminal to free space. Horn antennas are frequently used in microwave bands where the wavelengths are short enough to design a reasonably sized horn having an aperture width greater than the wavelength. A horn antenna appears with a waveguide port on one end, and flares out to some aperture at the other end. These horns can be pyramidal or conical in shape,

or take some more complicated structure. In general, the peak gain of a horn antenna is approximately proportional to its aperture divided by the square of the wavelength. An approximation for a the peak gain of an optimum gain antenna, which is the antenna with maximum gain for a given length, provided by [4] is

$$G = \frac{6.5A}{\lambda^2} \tag{2.18}$$

where A is the aperture area and λ is the operating wavelength. The antenna beamwidth is inversely proportional the square root of its peak gain.

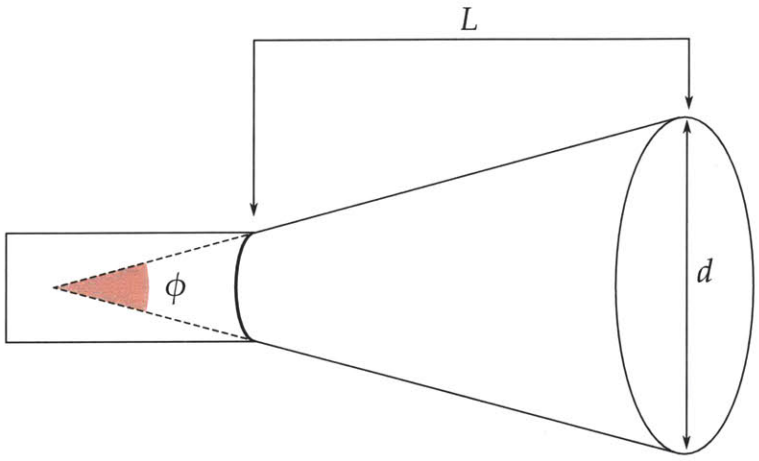

Figure 2-3: Cross-section geometry of a conical horn antenna. The feed port is on the left side, and the antenna has aperture diameter d, length L, and flare angle ϕ.

A conical horn is a horn antenna with a circular aperture, shown in Figure 2-3. It is principally characterized by two parameters: its length L and its aperture diameter d. These two parameters further define a flare angle as

$$\phi = 2 \arctan \frac{d}{2L}. \tag{2.19}$$

The flare angle has an impact on the shape of the phase front from the antenna. Generally this is desired to be as flat as possible, which would be the case with zero flare angle, but this does not provide optimum gain for a given antenna. The optimum gain conical horn of length L has a diameter of $d \approx \sqrt{3.125L\lambda}$ [23]. Realized gain is a compromise between the optimum-gain flare angle and the required phase front flatness.

A design innovation commonly seen in high performance horn antennas is the introduction of corrugations transverse to the horn flare on the interior wall of the horn. The corrugations are designed to have no effect on the boundary for radiation propagating straight out of the horn, but they reduce the propagation of radiation at other angles. Corrugated antennas are used when very low sidelobe levels are desired, typically in applications requiring a high beam efficiency. The downsides of corrugated horn antennas are their increased design complexity as well as manufacturing difficulties in cutting precise slots on the interior of a horn.

2.5.3 Matching the horn pattern to the reflector

To match a conical horn antenna to a reflector, we would first find the subtended angle β that fully illuminates the reflector. We would then determine the associated horn directivity required to produce sufficiently low gain at the edges of the reflector. This would determine the horn aperture diameter. If we were designing an optimum-gain horn we could then directly determine the length. If we required a flatter phase-front across the aperture we could elongate the horn, and if we wanted to produce a spherical phase-front we could actually shorten the horn. Since both the directivity of the horn and the parabolic reflector are dependent on wavelength, a system designed for one frequency is going to behave differently when operating at a different frequency.

2.6 NAST-M

The NPOESS Aircraft Sounder Testbed - Microwave (NAST-M) is multi-band total power microwave radiometer operating near 54, 118, 183, and 425 GHz. NAST-M operates as a cross-track scanning instrument, with four feeds (one for each frequency band) looking at a flat plate reflector. The four receivers are superheterodyne, with a single sideband in the 54 GHz band and double sidebands in the other three frequency bands. NAST-M has flown on several campaigns, and has been integrated into three high-altitude science aircraft: the NASA WB-57, the Scaled Composites Proteus, and the NASA ER-2. All three of these aircraft operate at altitudes between 17 km and 20 km [11]. NAST-M is intended to fly at sufficiently high altitude to measure through most of the atmosphere, providing a similar perspective to the satellite.

NAST-M provides equivalent coverage of ATMS channels 3 through 9 in the 54-GHz band and 18 through 22 in the 183-GHz band. The purpose of the 54-GHz channels is primarily for measurement of temperature with altitude, for altitudes up to about 13 km. The 183-GHz channels are to measure humidity at varying altitudes. Channels 10 through 15 are located around 57.3 GHz. These are not represented by NAST-M, due to the fact that their temperature weighting functions peak at altitudes between 17 km and 37 km. The missing channels are 10 through 15, which are located around 57.3 GHz, channel 16 at 89 GHz, channel 17 at 165 GHz, and finally channels 1 and 2 at 23.8 GHz and 31.4 GHz respectively [11, 14].

NAST-M has two external calibration reference loads: a thermally controlled hot load at $334.0\,\mathrm{K} \pm 0.1\,\mathrm{K}$ and an uncontrolled ambient load at $245\,\mathrm{K} \pm 5\,\mathrm{K}$. These two loads provide good reference points for calibration as they are approximately on either end of the typical brightness temperatures measured by the system. NAST-M has an additional port located at zenith on the scan to provide a measurement of the cosmic microwave background, as seen through the atmosphere from 17 km up [3].

NAST-M has a full-width at half-maximum beamwidth of 7.5°, and is capable of scanning a swath 100 km wide below the aircraft. NAST-M has flown several campaigns, collecting data over Hurricane Bonnie in 1998, underflying the NOAA-15 satellite to correlate data with AMSU in 1999 [1], as well as flying over convective regions in 2002 and 2003 [10].

Chapter 3

Aircraft Sensor Design and Development

The NPOESS Atmospheric Sounder Testbed - K-band (NAST-K) system is designed to be a fully independent passive microwave radiometer sensing near 23.8 GHz in K-band and 31.4 GHz in Ka-band. The system is designed to be deployed on an airborne platform—currently the project is designed for an initial campaign on the NASA ER-2 aircraft. The system uses a single feed horn antenna with a spinning parabolic mirror to reflect incoming radiation into the horn. The mirror is mounted at a 45° angle to the horn, and allows the system to view radiation in regions located cross-track to the aircraft longitudinal axis.

For this project I handled the majority of the system level design, with some guidance taken from the decisions made on NAST-M. I selected most of the components, and solicited designs for the radiometer front-end to produce a system compatible with ATMS. I did the preliminary mechanical layout of the instrument in both the WB-57, which was the original aircraft to be integrated, and later the ER-2. This included designing a preliminary model of the ER-2 wing pod from measurements I derived from photographs of the pod before actual measurements could be taken. The video amplifier was an original design I carried out for this project.

3.1 Overview

The NAST-K sensor can be divided into three major subsystems: the antenna system, the radiometer front-end, and the data acquisition system. Additionally, the sensor has several support systems including the power supply, flight computer, camera, and the voltage/temperature monitoring board. The block diagram in Figure 3-1 depicts all of the major components of the entire NAST-K system. The components of the antenna subsystem are the horn antenna, the parabolic reflector, and the scan drive motor. The radiometer front-end consists of the microwave frequency low-noise amplifiers, filters, references, and the video signal amplifiers. The data acquisition subsystem is a part of the flight computer, which contains integrated analog-to-digital converters (ADCs) for the sensor signals as well as the storage device for logging data.

NAST-K will sample each radiometer channel at a frequency of about 1 ksps, but the data can be integrated digitally over a longer period. An integration time of 100 ms will correspond to a angular range of 7.2° at the 0.2 Hz scan rate, smearing the signal over about the width of a spot. In the period of a single scan, the radiometer will have travelled about a kilometer, which means that the instrument will sample a given point in two consecutive scanning cycles. This ensures that the instrument covers the entire swath under the aircraft ground track.

3.2 Antenna assembly

The antenna assembly consists of a scanning parabolic reflector and a fixed horn antenna. The signal portion of the antenna assembly is described in detail in Chapter 4. The horn is mounted facing aft, mounted along the longitudinal axis of the aircraft. The reflector rotates the view by a fixed angle of 90°, aligning the boresight with the roll plane. The specific view direction is dependent on the reflector orientation. In the default position, the system looks at nadir through a port in the aircraft skin. The reflector can be spun by approximately 30° in either direction without the sensor view being occluded by the aircraft skin. The reflector can also be spun 180° to orient the sensor through another port at the zenith position. This configuration allows the sensor to look down at the earth and scan out a swath of approximately 60° perpendicular to the orientation of the aircraft. As the aircraft flies this swath can be further swept into a two dimensional region along the

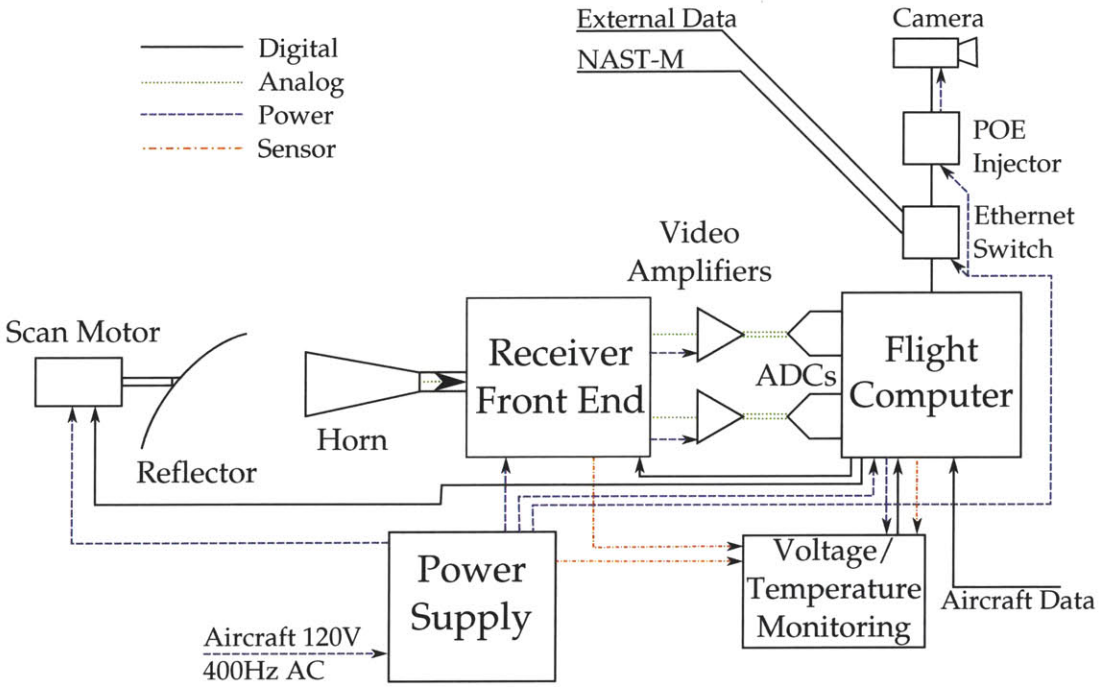

Figure 3-1: High-level block diagram of the NAST-K system.

aircraft ground track. The zenith port allows the sensor to look upwards to space in order to collect a reference signal associated with the cosmic microwave background.

The scan motor is a low temperature and low pressure rated stepper motor, attached to a digital controller to drive the motor, allowing the system to set a scan rate and read back absolute position, or set an absolute position. The stepper motor was chosen to be powerful enough to drive the reflector assembly directly, obviating the need for a gearbox. This simplifies the control of the reflector and increases pointing accuracy, reducing the backlash exhibited by a geared system. The scan assembly spins continuously as data is collected at a constant rate, except to correct for accumulated errors between the scan positions of the NAST-M and NAST-K reflectors. The spin rate is expected to be 0.2 Hz, consistent with the NAST-M scanner. Coupled with the corner frequency of 300 Hz for the receiver system (which corresponds to a 3-ms integration time) the angular "smearing" of the signal is expected to be around 0.3°, a minor distortion compared to the half-power beamwidth of approximately 7°.

Table 3.1: Radiometer front-end performance specification

Band	23.8 GHz	31.4 GHz
Center frequency	23.80 GHz $\pm$ 0.01 GHz	31.40 GHz $\pm$ 0.01 GHz
-3 dB bandwidth	270 MHz	180 MHz
Operating band	23.53 GHz to 24.07 GHz	31.22 GHz to 31.58 GHz
Stop band (≤ -40 dB)	$\leq$ 22.35 GHz	$\leq$ 29.98 GHz
	$\geq$ 25.25 GHz	$\geq$ 32.88 GHz
Noise figure	$\leq$ 3.7 dB	$\leq$ 3.7 dB
Passband ripple	$\leq$ 0.5 dB	$\leq$ 0.5 dB
within	23.655 GHz to 23.945 GHz	31.300 GHz to 31.500 GHz
Gain at detector input	$\geq$ 70 dB	$\geq$ 70 dB

3.3 Radiometer front-end (RFE)

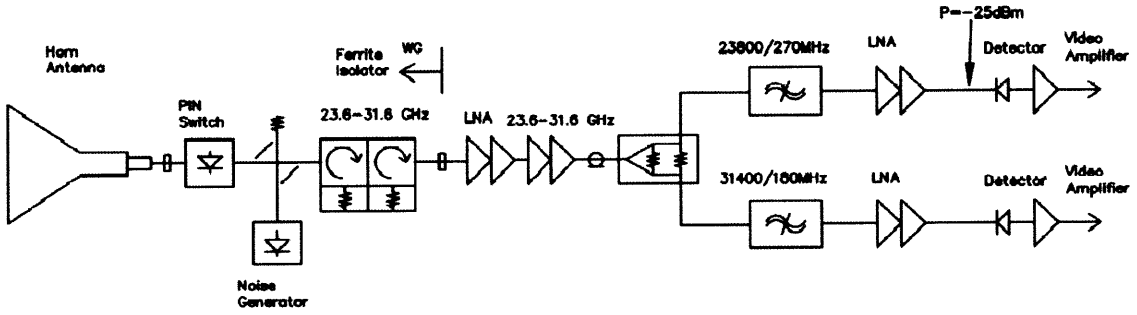

Figure 3-2: Block diagram of the radiometer front-end (RFE)[9]

The microwave components of the radiometer front-end were designed by Boulder Environmental Sciences and Technology (BEST) to MIT Lincoln Laboratory specifications. In our requirements [21] we requested two internal reference signals: a temperature controlled matched load and a noise diode. These signals are coupled into the receive path with a PIN diode switch and a directional coupler, respectively. Their design consists of a shared first stage LNA for both frequency bands, a power divider and filter bank to split the two bands, additional low-noise amplifiers, and finally a tunnel diode detector on each channel to rectify the microwave signal. The signals from the tunnel diode detectors are then passed to video amplifiers for additional filtering and amplification. A block

Table 3.2: Receiver noise equivalent delta-temperature (ΔT_{rms}) on NAST-K and ATMS. ATMS data is based on measurements presented in [5] and NAST-K data is based on expected noise figure and a 100 ms integration time.

	23.8 GHz band	31.4 GHz band
NAST-K Receiver Temperature (T_r)	389.8 K	389.8 K
NAST-K ΔT_{rms}	0.13 K	0.16 K
ATMS Measured ΔT_{rms}	0.25 K	0.31 K
ATMS Required ΔT_{rms}	0.5 K	0.6 K

diagram for the RFE up to the detectors is included in Figure 3-2.

Table 3.2 compares the expected performance of the NAST-K radiometer with the measured data from ATMS. Both NAST-K channels are expected to have lower ΔT_{rms} with a 100 ms integration time than ATMS. NAST-K's accuracy can be further increased by increasing the integration time, but this has the consequence of either enlarging the spots if the scan rate stays the same or causing gaps in the collected swath if the scanner is slowed down. Both NAST-K and ATMS are well within the ATMS specification of $\Delta T_{rms} = 0.5$ K at K-band and 0.6 K at Ka-band [14].

3.4 Video amplifier

The video amplifier was a custom design for this project. It takes the envelope of the microwave signal, which is provided by the tunnel diode detector, and amplifies this signal, low-pass filters the signal, and differentially buffers the signal for transmission to the analog-to-digital converter on the flight computer. The first stage of the video amplifier is an instrumentation amplifier, which provides an adjustable gain with a maximum DC gain of approximately 1000, and terminates the signal from the detector with the proper input impedance of approximately 160 Ω. The instrumentation amplifier also isolates the signal between the RFE and the flight computer in order to avoid a ground loop through the independent RFE and flight computer power supplies. The next stage is a first-order low-pass filter with a corner frequency of 300 Hz and a fixed gain of 10. The final stage is a differential driver with an effective gain of 3.3 and an optional passive first order RC

filter on the output. There is an adjustable offset reference which is the negative input for the differential driver. This allows the zero point of the differential signal to be adjusted over a range of 2.4 V. This is to provide some flexibility in order to maximize the utilization of the ADC input range. The two adjustable parameters are changed with the use of potentiometers. These potentiometers should be replaced with fixed value resistors in operation to avoid mechanical drift of the potentiometer wiper.

The video amplifier is powered by a bipolar $+5/-5$ V supply. The supply connections are bussed between adjacent video amplifier boards in the PCB layout to permit the use of multiple video amplifier boards with a single power supply connection. NAST-K uses two video amplifiers which are not connected to each other, so the amount of cross-talk that would be caused by bussed power connections has not yet been evaluated. The signal from the tunnel diode detector is fed in through an SMA connector. The power and output signal connections are provided through 0.1 in (2.54 mm) pin headers. The external dimensions of the board are 1 in by 2 in (2.54 cm by 5.08 cm). The video amplifier schematics and board layout are included in Appendix B.

3.5 System power and grounding

3.5.1 Power Conditioning Unit

NAST-K will include a new power conditioning unit (PCU) to supply power to the system. The PCU will include three outputs: a 28 V supply for digital electronics, a 18 V supply for the radiometer front end, and finally a 28 V supply for heaters and thermo-electric coolers. These supplies are separated in order to isolate the attached electronics from each other. A diagram of the power distribution is in Figure 3-3. The design of the PCU will be based on the NAST-M PCU. The decision was made to isolate the two power supplies in order to ensure that both instruments can still function independently.

3.5.2 Grounding

The general grounding design for the system is that of a star ground topology emanating from the PCU. A ground path will follow most electrical connections, but in cases where doing so would create a ground loop, some sort of isolation is provided. The Ethernet connections are automatically isolated through the use of isolation transformers

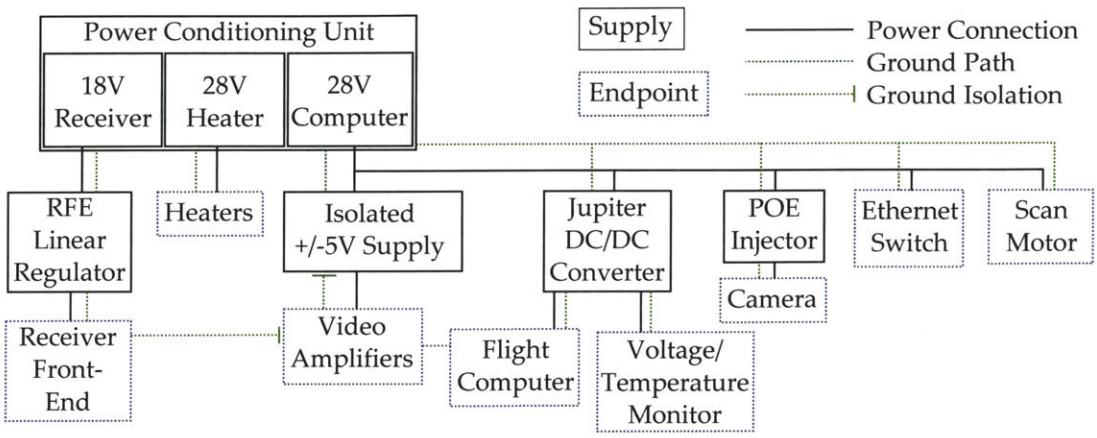

Figure 3-3: NAST-K power connections.

as required by the 100BASE-TX standard. The control signals for RFE components are optoisolated on the RFE side. Finally, the signal path from the RFE through the video amplifiers out to the flight computer had the potential for a ground loop, but this was mitigated by isolating the signal at the instrumentation amplifiers at the inputs of the video amplifiers. There is a very weak ground connection through a high value resistor between the two sides. Further, the power supply for the video amplifiers is itself isolated, ensuring that the ground reference for the video amplifiers is that of the flight computer and consequently the A/D converter.

3.5.3 EMI

The analog signals from the video amplifier are fed through individually-shielded twisted-pair cables. This is to minimize the possibility of external interference in the cable run between the RFE enclosure and the flight computer enclosure. In general, all enclosures should be metal-clad with metal shielded feed-throughs.

3.6 Flight computer

The NAST-K flight computer is responsible for collecting sensor data and controlling most of the other systems in the sensor. The flight computer has an on-board analog-to-digital converter which samples the outputs from the video amplifiers. It also collects temperature and voltage data from the monitoring board. It sends commands to the scan

motor assembly to control the reflector position. It also sends commands to the noise diode and PIN diode switch in the RFE in order to select the noise diode or matched load calibration references for regular instrument calibration. Finally, the computer records data from the aircraft bus, receives control signals from and transmits status signals to the aircraft, communicates with NAST-M for reflector synchronization, and operates the camera.

3.6.1 Hardware

The flight computer is a PC/104 form-factor single board computer with an 486 architecture CPU operating at 800 MHz with 256 MB of on-board DRAM, with a rated power consumption of 5.4 W. The computer is manufactured by Diamond Systems under the name Helios[8]. For our application we have added a 2 GB IDE flash drive, as well as a Compact Flash (CF) card. The board contains an integrated 16-bit 250 ksps self-calibrating analog-to-digital converter with 8 differential inputs (of which we are using two for the K- and Ka-band video amplifier signals). Additionally, the board has digital general purpose I/O (GPIO) lines, several serial ports, an on-board Ethernet adapter, and keyboard/video/mouse connections. The computer takes supply voltages of +5 V and +12 V which are provided by a power supply board connected to the PC/104 ISA bus. The power supply board takes a single +28 VDC input.

Figure 3-4: Flight computer enclosure I/O panel. [8]

One of the flight computer serial ports is being used for communication with the embedded environmental monitor (EEM) (see Chapter 5). Another will be used for communication with the aircraft data bus, as well as another to receive data from the NAST-M GPS module. The Ethernet connection allows for data retrieval on the ground, as well as communication with the camera and with NAST-M. The keyboard and mouse PS/2 ports as well as the VGA port are made available to operate the computer in the event that it is not functioning properly and is not reachable over the network. The GPIO lines are used to read the pilot control signal as well as to send power/fail status back to the pilot. Finally, several of the GPIO lines are fed to the RFE to control the PIN switch and noise diode output for periodic instrument calibration.

3.6.2 Operating System

The flight computer hardware is based on the x86 architecture, so we chose a general purpose Ubuntu Linux distribution on the computer. This would provide easy access to a variety of software as well as simple software development on a separate Linux-based computer. The normal server (no-GUI) version of Ubuntu Linux 10.04 was installed on the flight computer, but the processor could not boot the kernel due to lack of support for certain instruction set exceptions. This was resolved by compiling the kernel from source on the development computer and targeting it to the specific instruction set implementation of the CPU, and then replacing the installed kernel with the custom-compiled one. Compiling the kernel provided several advantages. First, we could remove support for a lot of unused hardware, reducing the required space considerably. We could add support for the specific hardware on our board, namely the A/D converter and the network card, both of which were not supported by the default kernel. Finally, we were interested in running our operational program at a real-time priority to guarantee timing performance, and we could accomplish this by enabling real-time extensions in the configuration.

There are two storage devices available on the flight computer. The IDE flash disk has the OS installed on it, and in operation will only be mounted read-only. This is accomplished by creating a RAM disk on system boot and using AUFS to lay the RAM disk over the read-only root file system. Any changes to root will be changed in the RAM disk and not the permanent disk. This operation is designed to be transparent to any software running on the operating system, so the software will be able to make changes

as usual. When the system is powered off, the RAM disk is lost, so upon reboot the OS will be back to its original state. This design protects the system from any corruption due to system crash or malfunctioning software. All science data will be stored on the CF card, which is writable. In the event of a system crash, the CF card may lose some data, but the software will make sure to push data out to disk quickly without significant buffering in order to minimize this potential loss.

3.6.3 Instrument Software

The operational software for NAST-K is designed to be able to start on system boot, so that setting up the instrument to collect data is as simple as turning on power. When the software starts, it will examine the system and prepare to start collecting data. It will send commands to the camera to start collecting images periodically. Once the camera is running and it has determined that the scan motor and RFE are working as expected, it will start driving the scan motor and collecting data. At certain places around the scan when the reflector is not pointed out either port, the computer will switch in the two references sources, and collect calibration data during every rotation. When the reflector crosses nadir it will command the camera to capture an image. The recorded sensor data is captured along with the aircraft position, altitude, orientation, and time, as well as the EEM data, and written out to disk.

NAST-K will proceed with these operations even if it hasn't received a signal that NAST-M is running yet. Once it determines that NAST-M is up, both instruments will ensure that the scanners are synchronized at a position where neither instrument is looking out a port or at a calibration load. This ensure that the motion will be smooth and consistent when crossing these regions. If the computer receives a shutdown signal from the pilot, the computer will immediately stop collecting data, turn off the RFE switches and noise diode, stop the camera, park the scan motor, and shut itself down. The PCU will be shut down soon after this signal is received, so the computer will soon be powered off even if it has crashed, although this may cause some data corruption.

3.7 Digital electronics

The remainder of the digital electronics include the camera, Ethernet switch and power-over-Ethernet injector, and the embedded environmental monitor. The camera provides a visual reference for the data being collected by capturing periodic visible-light images of the scene below the aircraft. The embedded environmental monitor measures voltages and temperatures to characterize the receiver operating points and help track down any issues with the instrument.

3.7.1 Camera

The camera is an off-the-shelf 1.3-megapixel digital video/still camera designed for building surveillance. The camera is the FS-IP1000 and is produced Sentry360[22]. It supports both video and still image capture up to 30 frames per second, and supports configurable image compression. It is controlled and transmits data over a standard Ethernet connection, and it is powered over the Ethernet connection (as specified in IEEE 802.3af-2003) at 48 V. The camera integrates a fish-eye lens over the sensor allowing for a 180° hemispherical view below the aircraft. A MicroSD memory card slot is located on board the camera for image data storage. This camera is intended to replace the NAST-M camera system, which consists of a CCD camera with custom wide-angle optics and an analog output, a frame-grabber card and PC/104 computer for image capture, along with an additional camera power supply. The system is being replaced in order to free up more room in the wing pod equipment rack, which may be taken up by the new NAST-K power conditioning unit, but the new camera has the additional advantage of producing a wider-angle and higher quality image.

When the sensor is operating, the camera is initially configured by the flight computer and commanded to periodically capture images. Each captured image will provide a hemispherical view of everything below the aircraft, so images could be captured as infrequently as once per rotation (every 5 seconds). This would correspond to the aircraft moving about 1 km which is significantly smaller than the spot size of the antenna. To avoid imposing a potential processing burden on the flight computer, the camera stores the images locally to be retrieved on the ground rather than sending them to the flight computer. This processing burden was the reason that NAST-M required a separate

computer for the old camera system.

3.7.2 Ethernet

Primary communication with NAST-M/K on the ground takes place over Ethernet, and there are several Ethernet connections on board the system. An Ethernet switch is located with the flight computer which communicates with the NAST-K flight computer, the NAST-M flight computer, the camera, and an external port for on the ground data access from all three systems. In addition to the switch is a power-over-Ethernet injector, providing a 48 V output on the segment with the camera in order to power the camera. Both the switch and power-over-Ethernet injector are powered off of the same 28 V DC supply.

3.7.3 Embedded Environmental Monitor

The embedded environmental monitor (EEM) is responsible for reading various supply voltages in NAST-K as well as temperatures of various sensor components. The housekeeping board is described in detail as a general purpose environmental monitor and data processor in Chapter 5. In the case of NAST-K we are most interested in the supply voltages for the low-noise amplifiers in the RFE, as well as the temperatures of the matched reference load, low noise amplifiers, and the band pass filters. These components are thermally regulated, but have varying performance over temperature so it is important to externally monitor their state to help justify the validity of the data and aid in calibration. The EEM periodically samples each of the 8 voltage inputs and 12 platinum resistance thermometers and sends the data over an RS-232 connection to the flight computer.

3.8 Electrical integration

3.8.1 NAST-M

NAST-K communicates with NAST-M to provide several functions. NAST-K attempts to synchronize its reflector scan as well as its data integration timing with NAST-M in order to produce coincident spots of data. Additionally, NAST-K relies on the Global Positioning System (GPS) receiver of NAST-M to record position and time information,

since this has been found to be more accurate than the GPS data available from the aircraft data bus. The bidirectional communication with NAST-K to determine scanner and data timing is provided by the Ethernet connection. The data coming from the GPS receiver is streaming out over a serial (RS-232) link. NAST-K listens to the same data stream as NAST-M and records the relevant data.

3.8.2 Aircraft Experimenter Interface Panel

The ER-2 experimental interface panel is used to provide power and communication with the aircraft systems. The data available over the experimenter interface panel includes pitch and bank, altitude, heading, GPS and ring laser gyro Inertial Navigation System (INS) data, time, as well as other aircraft status information. These data are available over individual digital interfaces as well as a single RS-232 connection[16]. For simplicity, NAST-K will utilize this RS-232 interface to record aircraft information. The most important pieces of information for NAST-K are the pitch, bank, altitude, and heading, since these affect the pointing direction of the antenna system. All data from the serial connection has a one second delay, which must be accounted for in the logged data. NAST-K receives a control signal from the pilot on this panel through a SPDT relay, allowing the pilot to shut the panel down in case of any problems. NAST-K returns a single digital signal to the pilot which extinguishes a fail lamp indicating that the instrument is operating properly. The experimenter interface panel provides two 3-phase 15 A 115 VAC 400 Hz circuits for powering the payload, as well as four +28 VDC circuits[16]. NAST-K will use one of the AC circuits to power the PCU.

3.9 Mechanical integration

NAST-K will be installed in the wing pod of the NASA ER-2, as depicted in Figure 3-5. The instrument will be mounted on the support rails that currently hold NAST-M with a frame cantilevered off the back. The equipment mounted to this frame includes the radiometer front-end and scalar feed horn, the flight computer and other digital electronics, the proportional-integral-derivative (PID) controllers for the heaters and thermoelectric coolers, as well as the scanning reflector assembly. The camera will be retrofitted into the existing cut hole intended for the old camera.

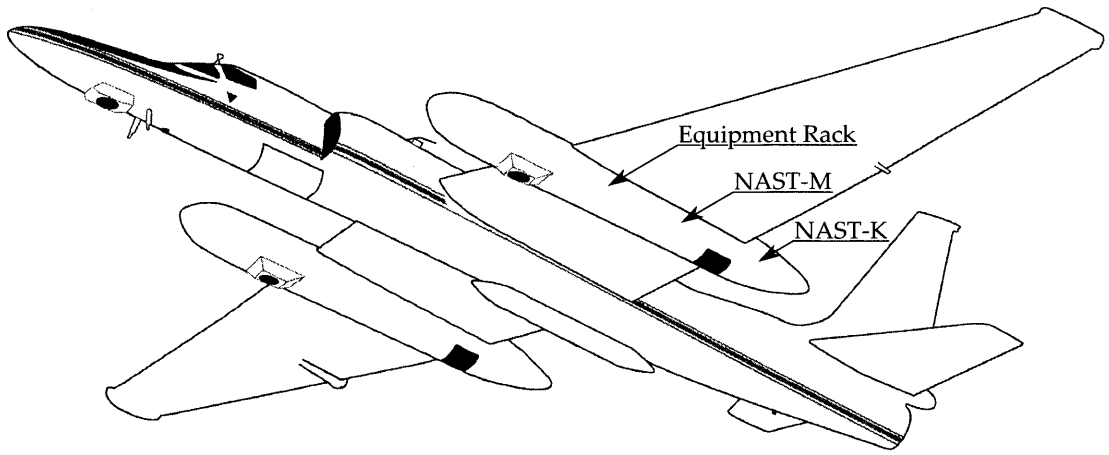

Figure 3-5: NASA ER-2 aircraft, isometric drawing. The labels depict the locations in the wing pod where NAST-M and NAST-K are installed, as well as the equipment rack for support equipment for the two instruments. The drawing is from [16].

3.9.1 Flight computer housing

The flight computer PC/104 stack will be located inside its own enclosure, which provides some protection for the printed circuit boards as well as a mounting bracket for the computer and a cover for the panel I/O interface (see Figure 3-4). This housing will be further enclosed in a housing which will provide the external barrel connections for the flight computer and other digital electronics. This enclosure will house the flight computer, the power-over-Ethernet adapter, the Ethernet switch, and the embedded environmental monitor board. The external connections on this housing include three IP68 rated barrel mount RJ-45 Ethernet connectors (one for the connection to NAST-M, one for the camera, and one to communicate with the computer on the ground), an interface cable to the PCU including power and aircraft data signals, an interface cable to the NAST-M GPS, as well as interface cables to the RFE and scan motor controller. The flight computer housing will include heating elements to prevent moisture buildup that could damage the electronics during descent.

3.9.2 RFE housing

The radiometer front-end will be mounted to a baseplate and located in a temperature controlled enclosure designed by Lincoln Laboratory. Figure 3-6 gives a top view of the enclosure. The enclosure includes all of the RFE components starting at an input waveg-

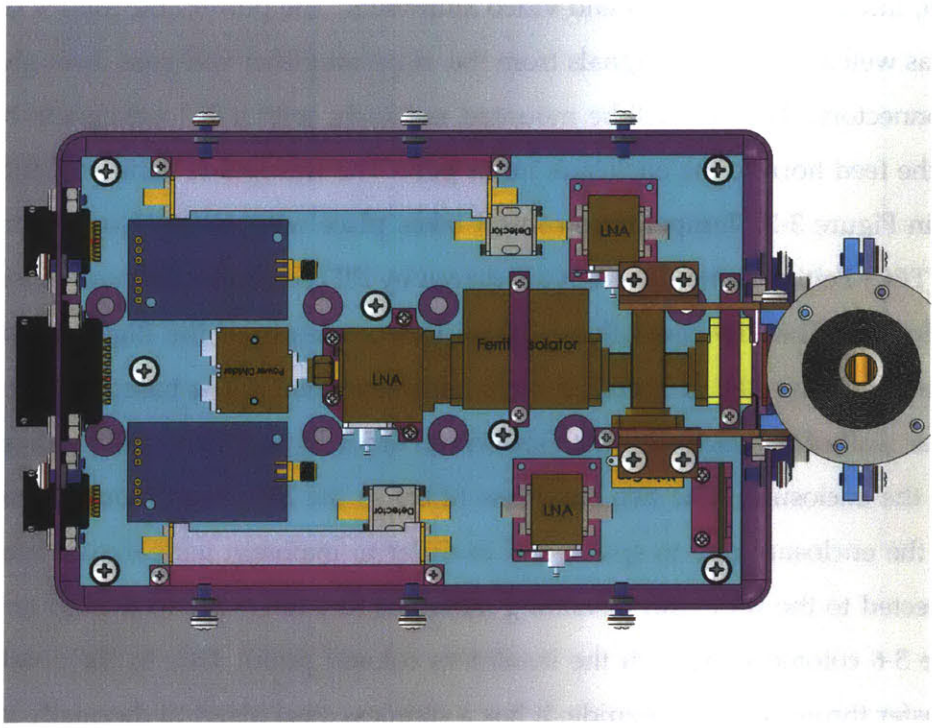

Figure 3-6: Radiometer front-end enclosure, top view. The feed horn is located on the right side of the drawing, and the barrel connectors are on the left.[6]

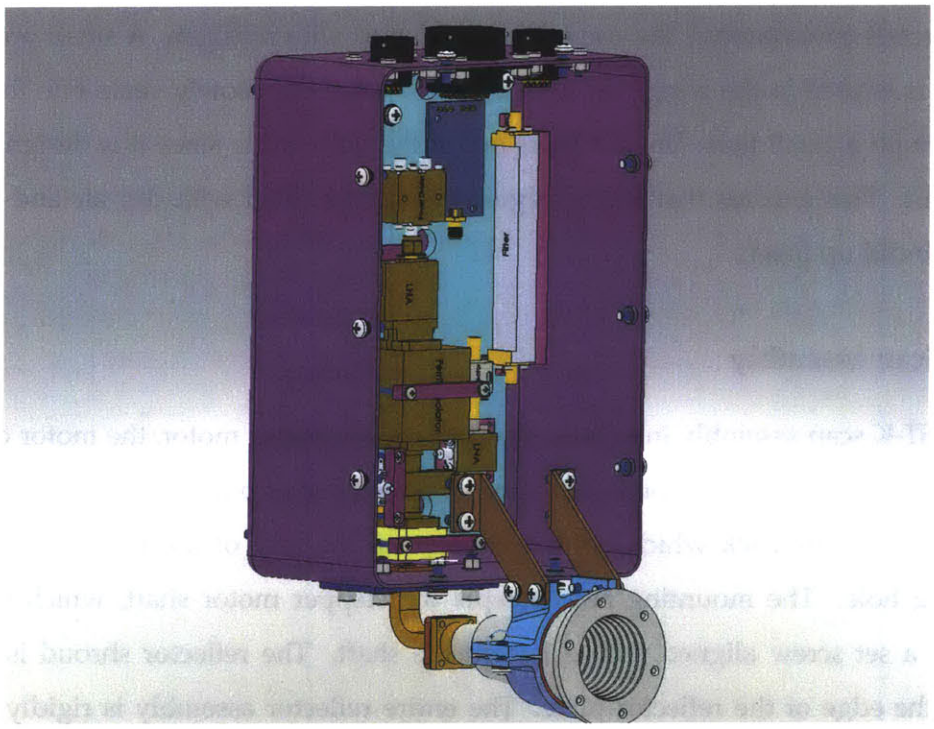

Figure 3-7: Radiometer front-end enclosure and feed horn. [6]

uide port, through the detectors and video amplifiers. The power and control signals for the RFE as well as the output signals from the video amplifier will pass through shielded barrel connectors. The box will be mounted vertically, with a 90° waveguide bend connecting the feed horn to the enclosure input port. The waveguide bend and antenna can be seen in Figure 3-7. Temperature control takes place with an array of thermo-electric cooling (TEC) Peltier elements which are driven by PID controllers located outside of the RFE enclosure. The PID controllers operate independently of the flight computer and simply maintain the RFE at specified temperature setpoints. The baseplate is connected to the rear wall of the enclosure with spacers in order to maintain isolation from the exterior of the enclosure. The two bandpass filters in the RFE were mounted to the side walls of the enclosure due to space, and in order to maintain temperature control they are connected to the wall with insulating materials (the filters are in the top and bottom of Figure 3-6 colored grey, with the insulators colored pink). Due to the possibility for heat transfer through the waveguide, it has a stainless steel insert to thermally isolate the PIN switch inside the RFE enclosure from the waveguide and antenna on the outside. This insert will reduce the heat conduction over the interface but maintain the electrically conductive surface inside the waveguide. In order to deal with the buildup of moisture in the aircraft environment, the waveguide is purged with nitrogen. A small pressurized cylinder is located in the wing pod with a needle valve that slowly vents into the waveguide through a small hole. The air leaks out of the waveguide since it is designed not to be airtight. This ensures that the waveguide is always filled with dry air and moisture will not build up inside.

3.9.3 Scan assembly

The NAST-K scan assembly integrates the scan drive stepper motor, the motor controller and driver, and the reflector plate and shroud. The reflector plate is attached to a mounting bracket on the back which holds the plane of the rear of the reflector at 45° to a mounting hole. The mounting hole accepts the stepper motor shaft, which is held in place by a set screw aligned with a flat on the shaft. The reflector shroud is attached around the edge of the reflector plate. The entire reflector assembly is rigidly attached to the motor shaft, so it should operate with no more backlash than is present in the motor itself. This design was chosen to maximize the pointing accuracy of the reflector

assembly, and to avoid additional mass and volume of the gearbox.

3.9.4 Aircraft integration

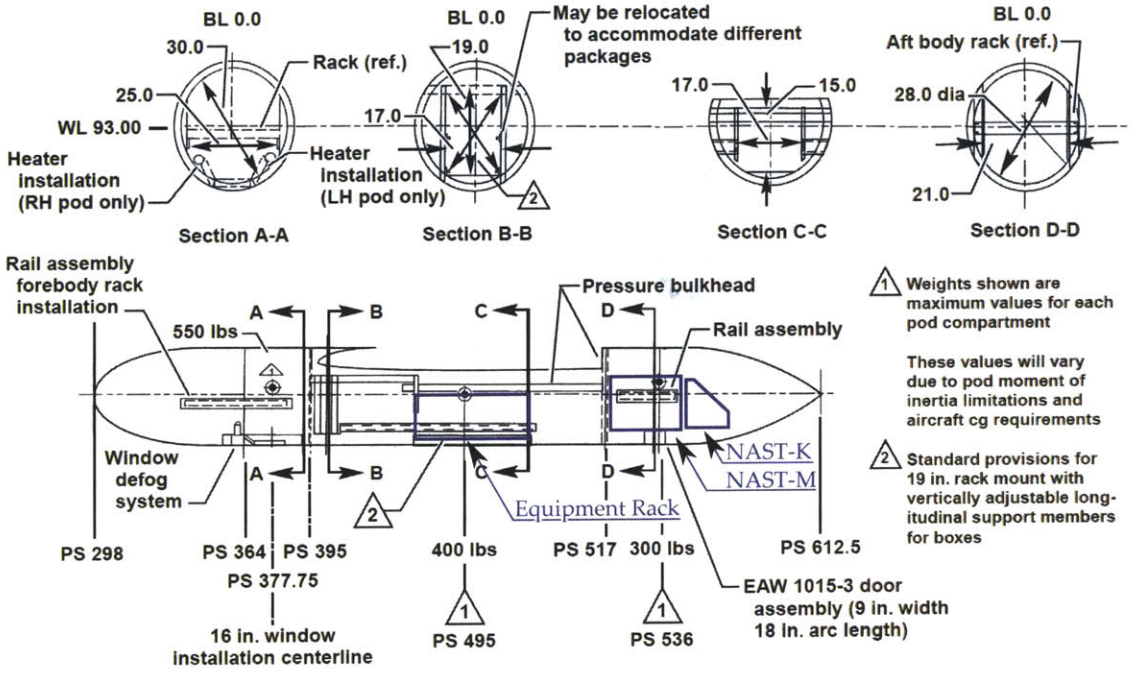

Figure 3-8: NASA ER-2 wing pod, side view with cross-sections. The approximate locations of the NAST-M and NAST-K instruments, as well as the support equipment rack are drawn over the side view. The drawing is from [16].

NAST-K equipment will be installed into the NASA ER-2 in two locations: the majority of the instrument will be located inside the wing pod aft cone, cantilevered off the support rails used by NAST-M, and the PCU and interface electronics will be located in the equipment rack. The environment in the wing pod aft cone is unpressurized, meaning that all of the equipment needs to be capable of operation in a low pressure and both high and low temperature environment. The operating temperature inside the pod can reach 70 °C when the aircraft is on the ground and drop to −40 °C when the aircraft is at altitude. Despite the low exterior temperatures, cooling may still be a concern as equipment generating heat cannot be effectively cooled through convection due to the low air pressure. In addition, when the ER-2 descends from altitude, the cold surfaces will cause water vapor in the air to condense and generate a large quantity of moisture. Any electronics in this area must be protected from moisture buildup, either through conformal

coating or through the use of heaters to prevent the electronics from becoming cold. The equipment rack is partially pressurized by the aircraft so these environmental issues are less of a concern.

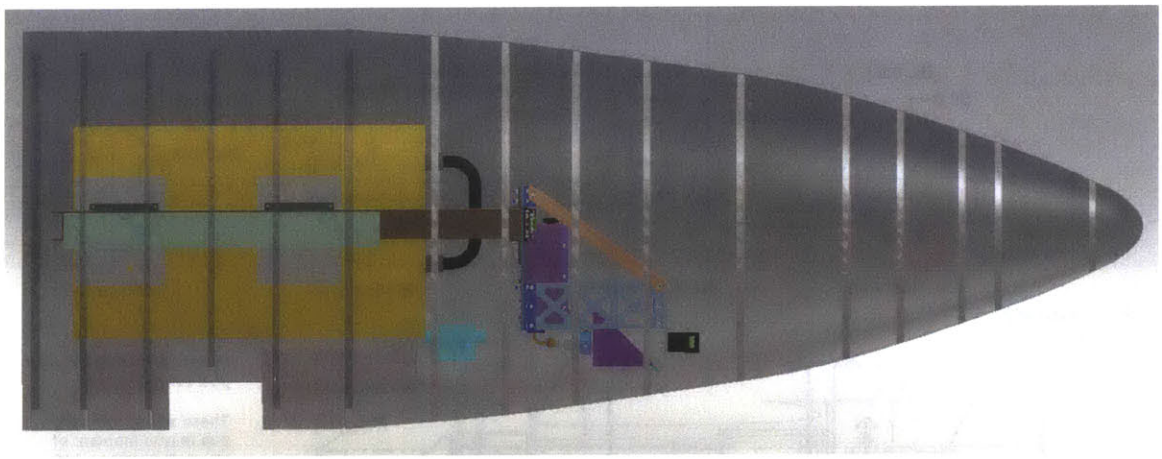

Figure 3-9: A side view of NAST-M and NAST-K in the aft wing pod of the ER-2. NAST-M can be seen in yellow and the smaller assembly mounted off of the brown support rails is NAST-K. The metal structural rings of the pod can be seen in white. [6]

The RFE enclosure is mounted vertically close to the back wall of NAST-M on a vertical plate. The waveguide port is at the bottom and the horn is pointed aft and held horizontally by a bracket attached to the RFE enclosure. There is a metal support frame attached to the vertical plate to hold the scan assembly. The longitudinal position of the entire assembly is a compromise between the moment arm created by moving the payload further out and ensuring clearance from NAST-M and its thermal radiating fins. The assembly also needed to be located such that the reflector could view between the structural rings of the aft cone. The reflector is located as close as possible to the wall of the cone to permit the maximum viewing angle range while still ensuring clearance as the reflector rotates.

3.10 Concept of operations

The NASA ER-2 is a high-altitude jet aircraft based on the United States Air Force U-2 reconnaissance plane designed by Lockheed. The aircraft operates at a cruise altitude between 60000 ft and 70000 ft (or 18 km to 21 km), and flies at a constant cruise airspeed of $210\,\mathrm{m\,s^{-1}}$. A typical mission will last about 5 hours at altitude [16]. This platform

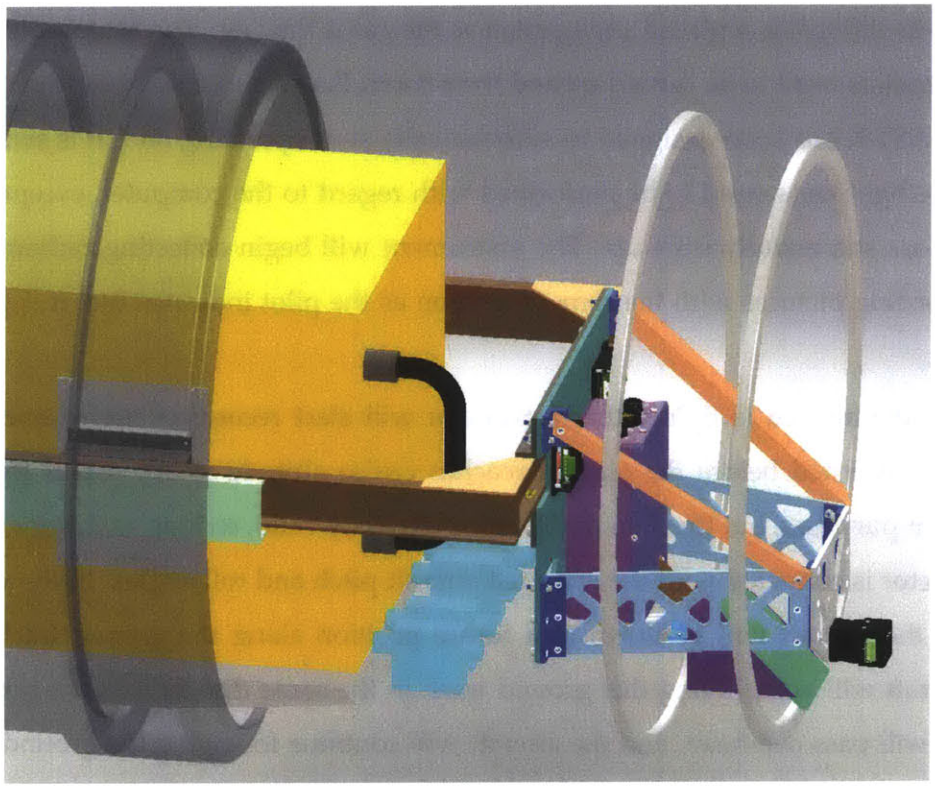

Figure 3-10: A close view of NAST-M and NAST-K in the aft wing pod of the ER-2. NAST-M can be seen in yellow and the smaller assembly mounted off of the brown support rails is NAST-K. The aft cone and some of the structural metal rings have been hidden for clarity. The two rings surrounding the reflector are still visible. [6]

allows for missions which cover a very large geographical area, and data can be collected thousands of miles from the aircraft home base.

In an operation, NAST-K will be fully integrated on to the aircraft. Once this is done, very little access to the instrument will be available, so all maintenance tasks need to be able to be performed quickly and without removing significant portions of the instrument. During pre-flight, the instrument must be checked for any objects which obstruct the full range of motion of the scanner. The nitrogen cylinder to purge the waveguide needs to be refilled or replaced and opened so the gas is flowing. The heaters and thermoelectric coolers need to be turned on and their controllers set to the appropriate temperatures. NAST-K has been designed to automatically start operating once it is switched on, so no preflight tasks need to be performed with regard to the computer, except to verify that it does successfully start up. The instrument will begin collecting radiometer data and recording pictures with the camera as soon as the pilot indicates that it is permitted to do so.

Once the aircraft is flying, the instrument will start recording useful science data. The data recorded before the aircraft reaches cruise altitude is not useful for satellite validation purposes, but the data itself will be perfectly valid, so long as the orientation of the reflector is corrected with the recorded aircraft pitch and roll angles. In the validation mission the aircraft will be flown to a future position along the ground track of NPP. The aircraft will begin flying this ground track in the same direction as the satellite, the satellite will pass overhead, and the aircraft will continue following the ground track for a period of time. The NAST-K swaths and the nadir ATMS spots will be cotemporal and colocated at one point, and will diverge in time in both directions. The most useful data will be that collected at the moment the satellite passed overhead, but data before and after this time remains useful as the atmosphere does not change rapidly at this scale. The NAST-M spots will be significantly smaller than ATMS, so a large number of them will be integrated to produce the ATMS spot. The NAST-M swath is designed to be wide enough to cover the zenith spot on ATMS.

After the aircraft is finished with the mission, it will descend and land. The instrument will be shut down at this point in order to protect it from substantial moisture collection during descent from the cold temperatures at altitude. Once the aircraft is on the ground, the flight computer and camera will be accessed using the Ethernet connection, and the

data will be stored. The mission data can then be cleared off of the two devices and they should be ready for use the next day. Preliminary analysis of the data will be performed immediately after removing it from the instrument, simply to verify that the system is still functioning properly.

Chapter 4

Antenna Subsystem

The antenna assembly for any passive microwave remote sensing system is designed to couple the energy from some far field region into the input to the receiver front end. In the case of NAST-K, the antenna system must focus energy from a circular spot in this far field region. The receiver will then measure average power of the spot integrated with respect to the antenna gain. The measured power is an accumulation of power radiated or reflected in the direction of the antenna by any matter in the projected cone of the spot. This spot can be thought of as an ellipse projected on the earth. The spot is circular when the antenna system is pointed down (at nadir), and also the smallest size, or highest resolution, in this position since it provides the shortest distance to the earth. As the look angle moves away from nadir, the spot becomes wider and more elliptical, as the intersection of the Earth's surface and the antenna cone takes place at a steeper angle. For extreme look angles or at high altitudes, the ellipse becomes distorted as the Earth's curvature becomes a significant factor. These factors place a limit on the utility of data collected at steep angles.

The NAST-K instrument measures power in two frequency bands: the first is 23.67 GHz to 23.94 GHz, referred to by the center frequency of 23.8 GHz and located in the IEEE K-band, and the second is 31.31 GHz to 31.49 GHz, centered at 31.4 GHz in the Ka-band. The K-band channels has a bandwidth of 270 MHz and the Ka-band channel a bandwidth of 180 MHz. The antenna system must be designed to operate at both of these frequency bands, ideally with comparable gain and beamwidth. The antenna system should have a high beam efficiency (greater than 95%) in both configurations.

The horn was designed to our beam specifications by Boulder Environmental Sciences and Technology (BEST). The original reflector was designed by Prof. Martinez at Northeastern University, who carried out a preliminary analysis[12]. I later modified the reflector design to meet our changing mechanical design and performed a new simulation to verify the expected performance. I also designed the reflector to be easily machined out of a plate of aluminum using a computer controlled milling machine. The analysis in this chapter is based on data about the horn provided to us by BEST which I integrated into my model for the horn and reflector system. The system was analyzed at the two operating frequencies and at a variety of viewing angles.

4.1 Design

The NAST-K antenna design incorporates a feed antenna, which couples the waveguide input to the receiver front end to free space, and a scanning reflector. The scanning reflector allows the feed antenna and consequently the entire receiver front end to remain fixed while the instrument's receive beam is moved. This simplifies the design because the only portion of the system which needs to move is the reflector. Scanning the entire system would require a much more powerful drive motor, more room in the aircraft, as well as many electrical feedthroughs to connect the rotating electronics to the fixed aircraft body. For optimum performance, the reflector should be oriented so that the received signal direction, or boresight, is at a right angle to the feed antenna. This allows the reflector to sweep out the largest arc as it rotates. Furthermore, the reflector should be oriented so that the scan is at a right angle to the flight direction of the aircraft. This produces the least overlap between spots as the aircraft moves, and consequently allows the instrument to collect data over the widest possible area.

4.1.1 Feed

The feed chosen for this design was a scalar conical horn antenna. The scalar feed horn provides nearly identical patterns in the E- and H-planes and very low sidelobe levels. This allows us to think of the feed as a simple Gaussian pattern, which lends itself to the idea of a projected "spot" on the ground. The original specification called for the horn to have a 25° $-3\,\mathrm{dB}$ beamwidth at $23.8\,\mathrm{GHz}$. This would represent a very wide beam, but

due to the space available in the aircraft we could not fit a significantly wider horn which could produce a smaller beam. This wide beamwidth was corrected with a parabolic reflector. Boulder Environmental Sciences and Technology (BEST) was chosen to design and fabricate the horn.

4.1.2 Reflector

The reflector design chosen was an offset parabolic reflector. A parabolic reflector is desirable because it can take a fairly broad feed and tighten it into a much narrower beam. Since the diameter of the feed is inversely related to the beamwidth, a broad-beam feed will be much smaller than a narrower-beam one. NAST-M used a flat plate reflector but operated at much higher frequencies, so a horn alone was sufficient to produce a narrow beam. In general we would desire as narrow a beam as possible, so long as the scan rate and aircraft speed were low enough that the spots on the ground were still oversampled. In the NAST-K design the sample rate is high enough that we are far from this being a design driver. Instead, the primary constraint on the size of the reflector is fitting it within the wing pod structure, and minimizing the moment of inertia of the reflector attached to the scan assembly. In the design, we achieved a reflector that was nearly as large as the spacing between metal structural rings in the wing pod. This reflector gives nearly the minimum possible beamwidth given the mechanical constraints without resorting to a multiple reflector design.

Fabrication

The reflector was modeled for fabrication in SolidWorks. The design of the reflector is shown in Figure 4-2. The reflector was designed to be fabricated out of a $1/2$ in (1.3 cm) aluminum plate. The parabolic shape would be milled to a surface tolerance of better than 0.19 mm, which is $\lambda/50$ for the shorter Ka-band $\lambda = c/31.4\,\text{GHz}$. To simplify the machining, the largest ball-end mill with a radius smaller than the smallest radius of curvature on the parabolic surface should be used. In this case, the radius of curvature is quite large, greater than 1 in, so a 1 in ball-end mill would likely be used. The parabolic reflector was designed to be balanced with the center of mass running through the shaft of the stepper motor. This was accomplished by pocketing the lower half of the backside of the reflector until the center of mass moved to the mounting axis. The reflector is

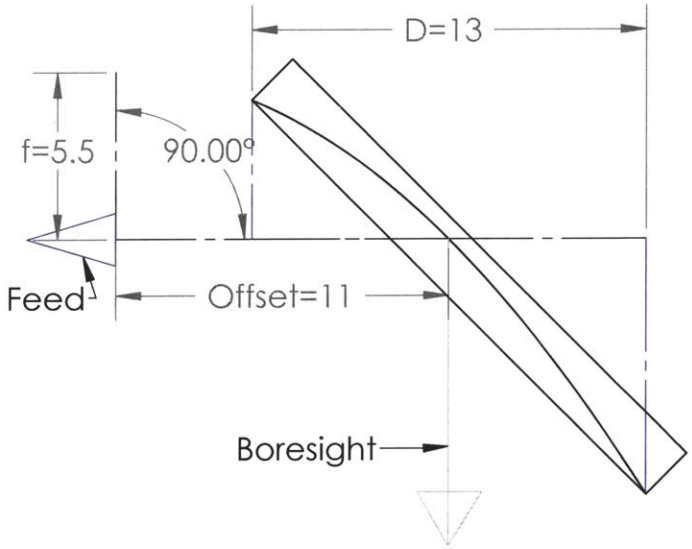

Figure 4-1: Profile drawing of the parabolic reflector (all dimensions are in centimeters).

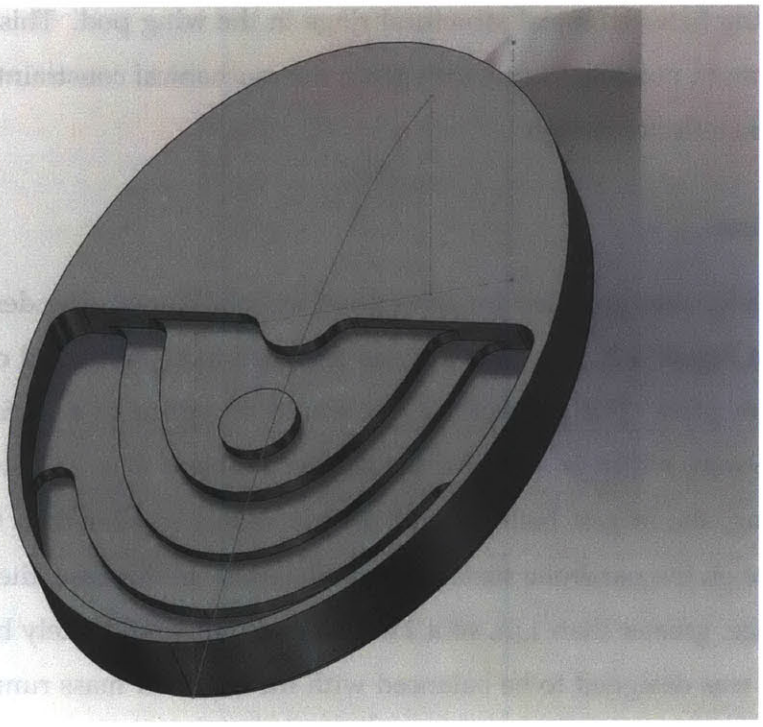

Figure 4-2: Solid model of the back of the parabolic reflector.

screwed on to a mounting bracket at three points. This mounting bracket holds the rear of the reflector plate at 45° to the motor axis and is mounted to the motor using a set screw holding the flat of the motor shaft.

4.1.3 Geometry

The reflector maintains a 90° angle between the feed axis and the boresight axis. This angle is chosen so that when the reflector spins about the feed axis the boresight remains in the cross-track plane, while the feed can remain stationary. The phase center of the feed is mounted at a distance of 11 cm from the center of the reflector (see Figure 4-1). At the (lower) K-band frequency our free space wavelength is $\lambda_K = 1.26$ cm, putting the feed distance at $8.7\lambda_K$. This keeps the reflector in the far field region of the feed, which simplifies the analysis of the system considerably. The reflector is designed with a 13 cm diameter circular rim, which provides approximately 1 cm of total clearance between the structural rings. The focal length of the paraboloid is 5.5 cm, giving an f/D ratio of 0.42.

4.2 Analysis

4.2.1 Conventions

The conventions used when describing the reflector system are depicted in Figure 4-3. The look angle from nadir is Ω. All of the far-field patterns are presented in spherical coordinates (θ, ϕ) around the boresight. The two principal polarization vectors for incident radiation $(\hat{u}, \hat{v})$ rotate with the boresight angle Ω. Thus, $\hat{u}$ and $\hat{v}$ form an orthogonal basis with the boresight vector $\hat{s}$. The principal polarization vectors for the feed are $\hat{x}$ and $\hat{y}$. Since the receiver system is linearly polarized in the $\hat{x}$ direction, the received signal corresponds to the electric field component E_x.

4.2.2 Horn antenna

The horn antenna was modeled using a full-wave simulation performed by BEST[24]. They used QuickWave-V2D with a model of the scalar feed design to calculate S parameters and far field radiation patterns. Their results gave a 3 dB full-width beam of 25° at K-band and 18.4° at Ka-band in the E-plane. The patterns were very circular, with the

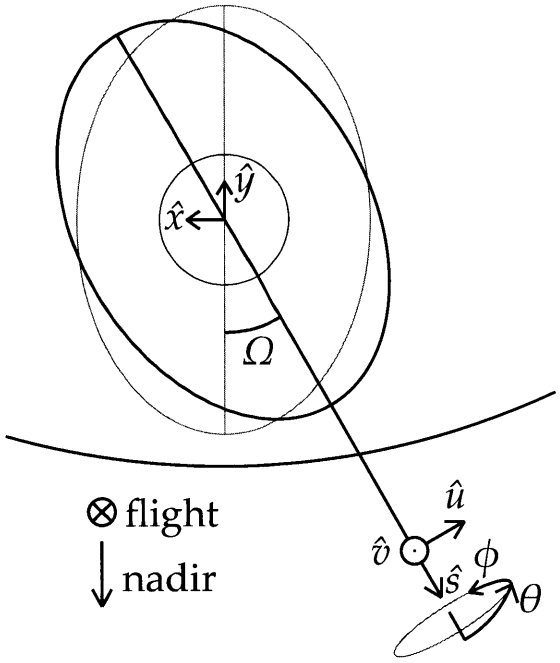

Figure 4-3: Geometric conventions for the reflector system. The view is looking in the forward direction of the aircraft. The nadir reflector position is shown as the light ellipse, and the current reflector position is the dark ellipse. The horn is depicted as a light circle.

H-plane beams measuring 24° at K-band and 18.8° at Ka-band. The peak sidelobe levels were −27 dB below the peak in both E- and H-planes at K-band, and in the H-plane at Ka-band. The E-plane had a higher sidelobe level of −23.5 dB. The S_{11} reflection parameter at the waveguide port was calculated to be −25 dB at K-band and between −45 dB and −54 dB at Ka-band. These data indicate that the horn and waveguide port are well impedance matched, with little reflected power on the output port.

4.2.3 Horn and reflector system

The feedhorn and reflector system was modeled using the General Reflector Antenna Software Package (GRASP) version 9.6.01 from TICRA. A Gaussian beam using the data provided by [24] was used to model the feed. This is a relatively accurate characterization for a scalar feed horn as the horn has very low sidelobe levels. The GRASP analysis was performed using both a flat plate and a parabolic reflector. The parabolic reflector was as designed, and the flat plate was modeled with the same rim as the parabolic, using a plane at a 45° angle to the feed axis. The flat plate is the design chosen in NAST-M,

and it also provides a good baseline for evaluating the performance of the parabolic. The analysis was performed at both 23.8 GHz and 31.4 GHz. The feed was modelled at each frequency as a Gaussian beam pattern with a beamwidth equal to that found by BEST. The horn sidelobe levels were over 20 dB below the peak and so they were neglected in the GRASP analysis. Thus, the analysis setup looked at a total of four configurations of the horn/reflector system, using both the K-band and Ka-band feeds, and both the flat and parabolic reflectors.

The GRASP analysis calculated the far-field response in a spherical coordinate system with the principal ($\theta = 0$) axis aligned with the boresight of the reflector. The far-field coordinate system was such that the $\phi = \phi/2$ plane was aligned with the direction of flight and the $\phi = 0$ plane remained coplanar with the cross-track plane. Far-field patterns were calculated out to $\theta = \pi/4$, giving a 90° full-width angle.

Further analysis was performed to ascertain the effect of reflector scan angle on the beam, specifically with relation to the polarization of the signal. The reflector was rotated cross-track as it would be in the operational system and far-field patterns were calculated at several look angles. The coordinate system for the far-field analysis remained aligned with the boresight of the reflector, as such it rotated with the reflector. The alignment was preserved so that the $\phi = 0$ plane was coplanar with the direction of flight and the $\phi = \pi/2$ plane was cross-track. At the nadir look configuration ($\Omega = 0°$), the primary electric polarization axis ($\hat{u}$) is horizontal, pointing along the horizon in the cross-track plane. The receiver is linearly polarized in the $\hat{x}$ direction, which corresponds to incident energy polarized along $\hat{u}$. When the reflector rotates to the horizon ($\Omega = 90°$), the primary electric polarization axis ($\hat{u}$) is now vertical, although the receiver polarization of $\hat{x}$ now corresponds to incident radiation along $\hat{v}$.

4.3 Performance

Several performance characteristics of the horn and reflector system were analyzed. First, the peak gain, beamwidth, and beam circularity were evaluated. Second, the beam efficiency was calculated using several different criteria and the relative merits of the criteria were considered. The beamwidth and beam efficiency data were used to calculate Earth spot sizes, which were compared with the resolution of NAST-M and ATMS. Finally, an

analysis was carried out to determine the effect of look angle on reflector polarization.

4.3.1 Beam shape

The beam shape was characterized by peak gain (relative to isotropic), and the full-width angles at the $-3\,\mathrm{dB}$, $-10\,\mathrm{dB}$, and $-20\,\mathrm{dB}$ contours relative to the peak gain. The beam circularity was characterized by finding the standard deviation of the full-width angle of constant-ϕ cuts over all ϕ. Since the feed is symmetric, any asymmetry in the pattern would be expected to result from the fact that an offset parabolic is necessarily asymmetric about one axis. In the case of the flat plate reflector, we would expect no change in the far field pattern from that of the feed itself, assuming the plate is large enough.

Results

The gain and beamwidths of the four system configurations are displayed in Table 4.1. Two-dimensional spherical gain patterns are shown in Figure 4-4. Perhaps the most interesting result is how close the gain and beamwidth are between the two reflector configurations. The feed displays the expected relationship between the beamwidths, where the ratio between the K- and Ka-band beamwidths is approximately the reciprocal of their frequencies. With the parabolic reflector, these beamwidths are far closer together, within 10% of each other. Since the reflector is designed to be illuminated by the horn at 23.8 GHz, it is thought that the tighter beam when the horn is feeding 31.4 GHz actually under-illuminates the reflector. This causes the effective aperture of the reflector to be smaller, thus decreasing the effective f/D ratio, nearly negating the varying beamwidths between the two frequencies.

4.3.2 Beam efficiency

Beam efficiency was calculated using the method described in [19]. In this case we define beam efficiency as the ratio of the power received via the main beam to the total power received by the system, where the main beam is defined using several different methods to be discussed in the next section. Beam efficiency is a metric for the quality of an antenna system: the signal from the main beam is the signal coming from the target of the antenna, whereas the remainder of the signal is from everywhere else. This unwanted

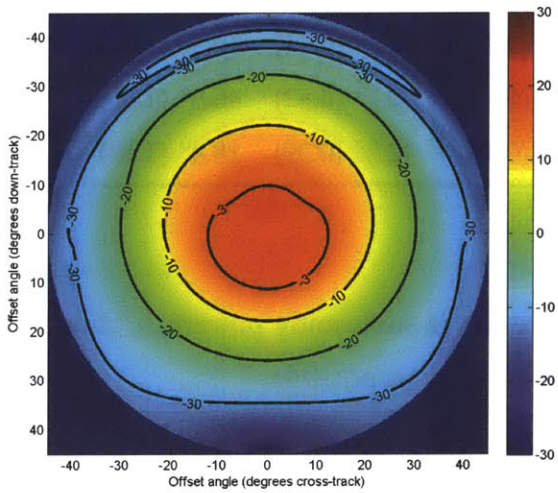

(a) K-band flat plate

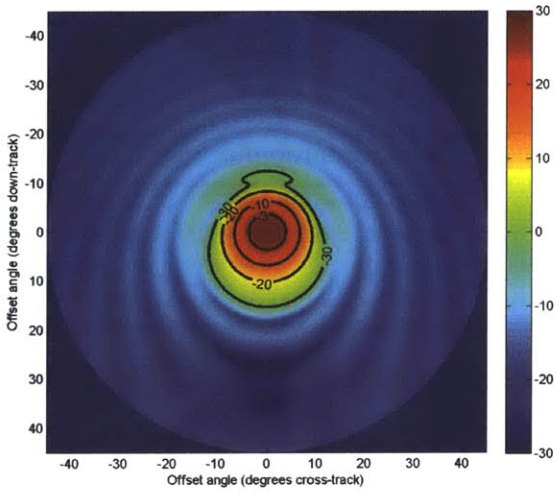

(b) K-band parabolic

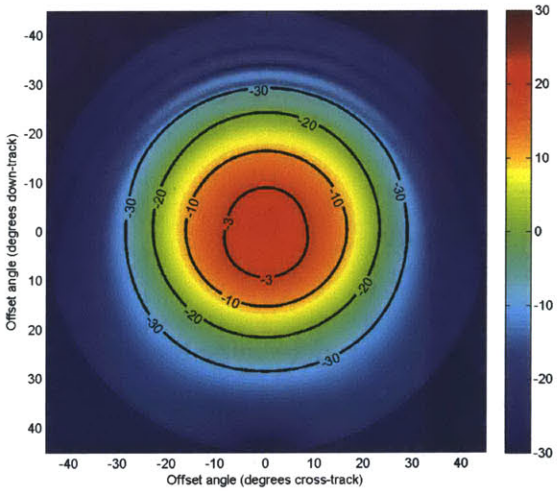

(c) Ka-band flat plate

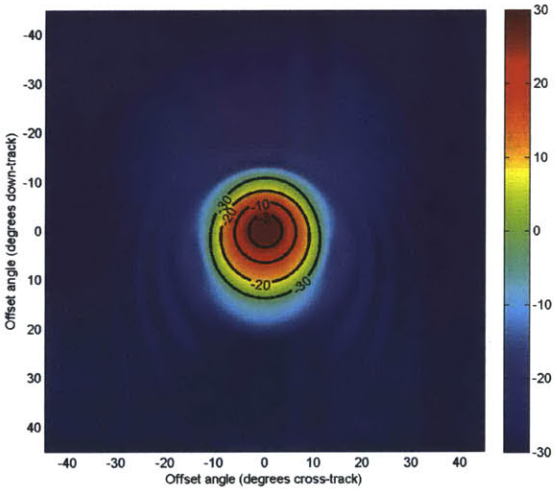

(d) Ka-band parabolic

Figure 4-4: Antenna gain for the four reflector configurations (flat/parabolic, K-/Ka-band) measured in dBi. The plot center is boresight, and the coordinates are polar as described in Section 4.2.1 with the distance from the center representing θ and the rotation angle ϕ. Contours are placed at -3, -10, -20, and -30 dB from the peak

Table 4.1: Beamwidth for flat plate and parabolic reflectors at −3, −10, and −20 dB cutoffs

	Peak gain	−3 dB	−10 dB	−20 dB
K-band flat	18.3 dBi	25.8°[a] (3.35)[b]	42.6° (3.80)	61.0° (4.85)
K-band parabolic	28.2 dBi	7.42° (0.11)	13.2° (0.31)	18.5° (1.36)
Ka-band flat	20.7 dBi	18.8° (0.66)	32.7° (0.82)	46.5° (1.66)
Ka-band parabolic	28.8 dBi	6.83° (0.18)	12.5° (0.39)	18.4° (1.68)

[a] mean full-width angle
[b] standard deviation of full-width angle

signal can be a significant source of interference if it is sufficiently powerful. Thus, it is desirable to maintain a beam efficiency as close to unity as possible.

Method

With the antenna gain function $G(\theta, \phi)$ normalized such that

$$\frac{1}{4\pi} \int_0^{\pi} \int_0^{2\pi} G(\theta, \phi) \sin\theta \, d\phi \, d\theta = 1, \tag{4.1}$$

we can compute beam efficiency as the integral

$$\eta = \frac{1}{4\pi} \iint_{beam} G(\theta, \phi) \sin\theta \, d\phi \, d\theta. \tag{4.2}$$

The conditions on the integration limits in the equation above determine the precise definition of the beam efficiency being found. Since the projected spot associated with the antenna system is generally considered to be the -3 dB beam width, the -3 dB contour might be used as the limit of integration. This metric would indicate how much of the measured signal originated from within the projected spot. Another metric is to determine the contour of the first null in the antenna pattern, and use that as the limit of integration. Since the first null may be difficult to accurately characterize, a standard of an angle 2.5 times larger than the -3 dB beam width is proposed by [19]. This method is relatively agnostic to the specific roll-off of the beam so it may be preferable.

Beam efficiency was calculating using the standards described above. Furthermore, the first standard, the -3 dB beam efficiency, is found using two separate methods. The

first method, using the region where the antenna gain is greater than half of the peak, is simply

$$\eta_{-3\,\mathrm{dB}} = \frac{1}{4\pi}\int_0^{2\pi}\int_0^{\theta_{-3\,\mathrm{dB}}(\phi)} G(\theta,\phi)\sin\theta\,d\theta\,d\phi. \tag{4.3}$$

The second method integrates out to the same θ over all ϕ, where the maximum θ is the mean of the half-power angles over all ϕ, or

$$\bar{\theta}_{-3\,\mathrm{dB}} = \frac{1}{2\pi}\int_0^{2\pi} \theta_{-3\,\mathrm{dB}}(\phi)\,d\phi. \tag{4.4}$$

With this angle, the beam efficiency can be found as

$$\eta_{\angle -3\,\mathrm{dB}} = \frac{1}{4\pi}\int_0^{2\pi}\int_0^{\bar{\theta}_{-3\,\mathrm{dB}}} G(\theta,\phi)\sin\theta\,d\theta\,d\phi. \tag{4.5}$$

The next standard is very similar to the second method of the half power standard, except the integration of θ is carried out to an angle of $2.5\bar{\theta}_{-3\,\mathrm{dB}}$. Thus, the beam efficiency here is

$$\eta_{2.5\angle -3\,\mathrm{dB}} = \frac{1}{4\pi}\int_0^{2\pi}\int_0^{2.5\bar{\theta}_{-3\,\mathrm{dB}}} G(\theta,\phi)\sin\theta\,d\theta\,d\phi. \tag{4.6}$$

The final standard is to integrate along θ out to the first null. This is found by solving $\frac{\partial G}{\partial \theta}(\theta,\phi) = 0$ for θ in terms of ϕ (and taking the smallest value of θ). If we denote this $\theta_n(\phi)$, then the formula for beam efficiency becomes

$$\eta_{full} = \frac{1}{4\pi}\int_0^{2\pi}\int_0^{\theta_n(\phi)} G(\theta,\phi)\sin\theta\,d\theta\,d\phi. \tag{4.7}$$

Results

From Table 4.2 we can see some useful results. First, perhaps as expected, the $-3\,\mathrm{dB}$ (half power) metrics are extremely poor for representing the beam. In all configurations, only about half of the received signal comes within the $-3\,\mathrm{dB}$ contour. There is no appreciable difference between using the mean angle and exact contour for the half power beam efficiencies. The greatest difference is in the Ka-band parabolic configuration, which exhibits a 4% deviation. The wide angle metric ($\eta_{2.5\angle -3\,\mathrm{dB}}$) turns out to be a very good metric for evaluating the beam efficiency. In the worst case, over 93% of the received signal is contained in this region, and in the other cases, over 96% of the signal is covered. This is not as complete as using the first null contour, but this is not well defined in the

Table 4.2: Beam efficiency for the flat plate and parabolic reflectors

	$\eta_{-3\,\mathrm{dB}}$	$\eta_{\angle -3\,\mathrm{dB}}$	$\eta_{2.5\angle -3\,\mathrm{dB}}$	η_{null}
K-band flat plate	0.543	0.537 (25.6°[a])	0.934 (64.0°)	—[b]
K-band parabolic	0.482	0.479 (7.4°)	0.960 (18.5°)	0.976
Ka-band flat plate	0.511	0.514 (18.6°)	0.978 (46.5°)	—
Ka-band parabolic	0.472	0.455 (6.8°)	0.971 (17.0°)	0.998

[a] full-width beamwidth used to find beam efficiency.
[b] flat plate configurations do not have a well defined null.

case of flat reflectors due to the lack of appreciable sidelobes. Furthermore, a circular region is preferable as it lends itself to a circular spot on the ground. From these data, it is believed that $2.5\theta_{-3\,\mathrm{dB}}$ is a good cutoff to define the circular spot for any of the system configurations.

Regarding the performance of the parabolic reflector, we find that at both frequencies the beam efficiency is good, with over 96% of the power being contained in $\theta < 2.5\theta_{-3\,\mathrm{dB}}$. The beam efficiency when using the parabolic reflector is either slightly better or approximately the same when compared to the flat plate reflector. Furthermore, the parabolic reflector is the only option that meets the 95% beam efficiency design goal.

4.3.3 Projected spot size

The spot of a pencil beam refers to the size of the beam as projected on some surface. We are interested in finding the size of the beam as projected on the Earth's surface, and the variation in this size as the look angle moves from nadir out toward the horizon. At nadir a circular beam will produce a circular spot on the earth, and as the look angle moves out towards the horizon the spot will become elliptical, with the major axis along the look direction and the minor axis perpendicular.

Method

The geometry used in calculating the project spot size is shown in Figure 4-5. In our model we find the point at which boresight intersects with the Earth's surface and project the spot onto a tangent plane to the Earth at this point. The Earth is modelled as a smooth sphere. As such, there are two major sources of error. The first is the distortion of the spot from a true ellipse due to the curvature of the Earth near the intersection point. This is only a significant issue when the spot size is significant compared to the size of the Earth. The second error is due to the asphericity of the Earth, as well as the variation in elevation along the surface.

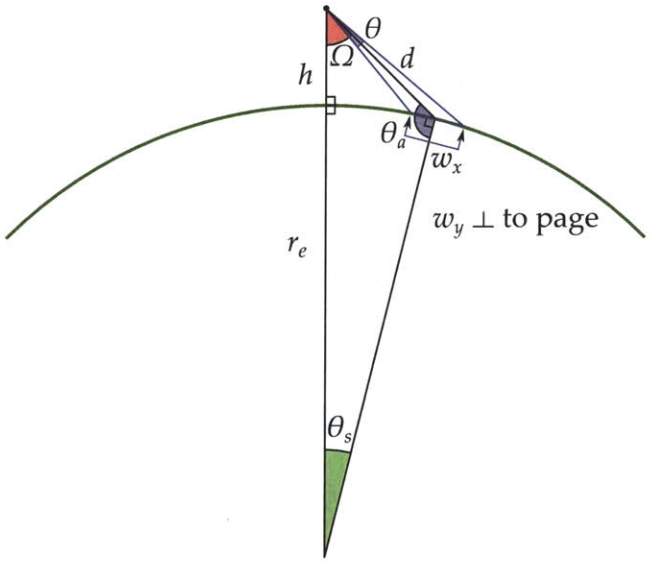

Figure 4-5: The geometry necessary to find the projected spot size of a beam on the earth. h is the altitude of the sensor, Ω is the look angle from nadir, θ is the full-width beamwidth, and r_e is the Earth's radius. The calculated values are d, the distance from the sensor to the Earth's surface along boresight, and w_x and w_y, the major and minor axis spot diameters.

We are interested in finding the dimensions of the spot ellipse w_x and w_y. We first calculate the distance d between the sensor and the surface of the Earth along boresight. First, using law of sines we find the angle θ_a with

$$\frac{\sin\theta_a}{r_e + h} = \frac{\sin\Omega}{r_e}. \tag{4.8}$$

Since θ_a is always in the second quadrant, we find its value as

$$\theta_a = \pi - \arcsin\left(\frac{r_e + h}{r_e}\sin\Omega\right). \tag{4.9}$$

Given the angle θ_a we can then find the subtended Earth angle between the sensor and the spot θ_s as

$$\theta_s = \pi - \Omega - \theta_a. \tag{4.10}$$

Using the law of sines again we find the distance d using

$$\frac{\sin\theta_s}{d} = \frac{\sin\Omega}{r_e}. \tag{4.11}$$

Combining these formulas we can find

$$d = \frac{r_e \sin\theta_s}{\sin\Omega} = \frac{r_e \sin(\pi - \theta_a - \Omega)}{\sin\Omega} \tag{4.12}$$

$$= \frac{r_e \sin\left(\arcsin\left(\frac{r_e+h}{r_e}\sin\Omega\right) - \Omega\right)}{\sin\Omega} \tag{4.13}$$

$$= (r_e + h)\cos\Omega - \sqrt{r_e^2 - (r_e + h)^2 \sin^2\Omega}. \tag{4.14}$$

Once we have solved for d we can find the minor axis diameter w_y. This is simply the width of the beam perpendicular to boresight at distance d, or

$$w_y = 2d\tan\frac{\theta}{2} \tag{4.15}$$

where θ is the full beamwidth. We can use the altitude angle θ_a to find the major axis width w_x as

$$w_x = w_y \csc\left(\theta_a - \frac{\pi}{2}\right) = -w_y \sec\theta_a = -2d\tan\frac{\theta}{2}\sec\theta_a. \tag{4.16}$$

Results

As we can see from Table 4.4, NAST-M/K has a substantially smaller spot size than all of the ATMS channels due to the significantly lower altitude of the airborne platform. All of the NAST-M/K beamwidths are wider than ATMS beamwidths, but the altitude difference results in spots around an order of magnitude smaller in diameter. Comparing NAST-K and the corresponding ATMS channels 1 and 2, NAST-K has spots 34 times

Table 4.3: Distance from instrument to the Earth's surface along boresight (d) for NAST-M/K and ATMS at nadir, $\Omega = 24°$, and $\Omega = 48°$.

Instrument	Altitude	$\Omega = 0°$	$\Omega = 24°$	$\Omega = 48°$
NAST-M/K	18 km	18 km	19.6 km	26.6 km
ATMS	824 km	824 km	914 km	1350 km

Table 4.4: Spot size comparison between NAST-K, NAST-M, and ATMS at nadir, $\Omega = 24°$, and $\Omega = 48°$. Spot size is circular at nadir, and at other angles it is displayed as $w_x \times w_y$. ATMS beamwidths and altitude from [14], NAST-M beamwidth from [11].

Instrument	-3 dB Beam	$\Omega = 0°$	$\Omega = 24°$	$\Omega = 48°$
NAST-K K-band	7.4°	2.3 km	2.7 km × 2.5 km	5.2 km × 3.5 km
NAST-K Ka-band	6.8°	2.1 km	2.5 km × 2.3 km	4.8 km × 3.2 km
NAST-M	7.5°	2.3 km	2.8 km × 2.5 km	5.3 km × 3.5 km
ATMS Chs. 1,2	5.2°	75 km	93 km × 83 km	225 km × 123 km
ATMS Chs. 3-16	2.2°	32 km	40 km × 35 km	95 km × 52 km
ATMS Chs. 17-22	1.1°	16 km	20 km × 18 km	48 km × 26 km

smaller in diameter, for an effective areal resolution nearly 1200 times greater than ATMS. This means that about 1200 NAST-K spots would collected to cover a single ATMS spot. At an extreme look angle of 48°, the NAST-K spots are 37 times smaller in the major axis and 46 times smaller in the minor axis, for a spot area 1700 times smaller than ATMS. This increase is in difference comes about because the Earth's curvature is a much more significant factor at the altitude of ATMS. NAST-K is capable of collecting data which would be invisible to ATMS due to the difference in spot size. This positions NAST-K as a useful platform for collecting science data in addition to its primary satellite validation mission.

4.3.4 Polarization

Antenna polarization is a relevant metric in atmospheric sensing systems, as many of the phenomena of interest produce polarized radiation. When the antenna is pointed at nadir, the so-called horizontal and vertical polarizations are orthogonal, but essentially the same. Their orientation is entirely dependent on the direction the aircraft is flying. This does not mean that a received signal will be equally polarized in both bases, but rather that the polarization of incident radiation will depend entirely on the direction the aircraft is pointed. If the antenna is pointed off nadir, the two polarizations take different meanings as one becomes horizontal and the other vertical relative to the earth. At a look angle of 90°, the vertical and horizontal polarization vectors associated with the horn will be matched with the vertical and horizontal polarization vectors of radiation incident on the system.

Method

To determine the effect of look angle on the antenna system polarization, the system was evaluated using the four feed/reflector configurations with look angles spaced 15° from nadir to horizon. The spherical E-field cuts were used to calculate the four Stokes

parameters (I, Q, U, V) as a function of (θ, ϕ) with

$$I = |E_u|^2 + |E_v|^2, \tag{4.17}$$

$$Q = |E_u|^2 - |E_v|^2, \tag{4.18}$$

$$U = 2\,\mathrm{Re}(E_u E_v^*), \tag{4.19}$$

$$V = 2\,\mathrm{Im}(E_u E_v^*). \tag{4.20}$$

We further define the complex linear polarization as

$$L = Q + iU, \tag{4.21}$$

and the total polarization as

$$I_p = \sqrt{Q^2 + U^2 + V^2}. \tag{4.22}$$

These give us the elliptical polarization parameters

$$A = \sqrt{\tfrac{1}{2}(I_p + |L|)}, \tag{4.23}$$

$$B = \sqrt{\tfrac{1}{2}(I_p - |L|)}, \tag{4.24}$$

$$\psi = \tfrac{1}{2}\arg(L), \tag{4.25}$$

where $\arg(C)$ is the argument function, or the polar angle associated with complex number C [13]. A visual representation of these parameters is depicted in Figure 4-6. The major axis magnitude A is the peak electric field magnitude over the period of the wave. The minor axis magnitude B is the electric field magnitude 90° out of phase with the peak. The angle ψ is the rotation of the polarization ellipse, which is the dominant polarization direction of the signal. The circular polarization direction (left or right hand) can be found as $h = \mathrm{sgn}(V)$. Our receiver is intended to be linearly polarized, so the eccentricity, or B/A, gives us a metric of how much the polarization is distorted from linear. A value of 0 represents a linearly polarized wave, and a value of 1 is a perfectly circularly polarized wave.

The two parameters of most interest to us are the eccentricity, B/A, and the major axis angle, ψ. In the high gain region of the system, we would like to have an eccentricity near zero, indicating a linearly polarized signal, and we expect ψ to be equal to the look angle

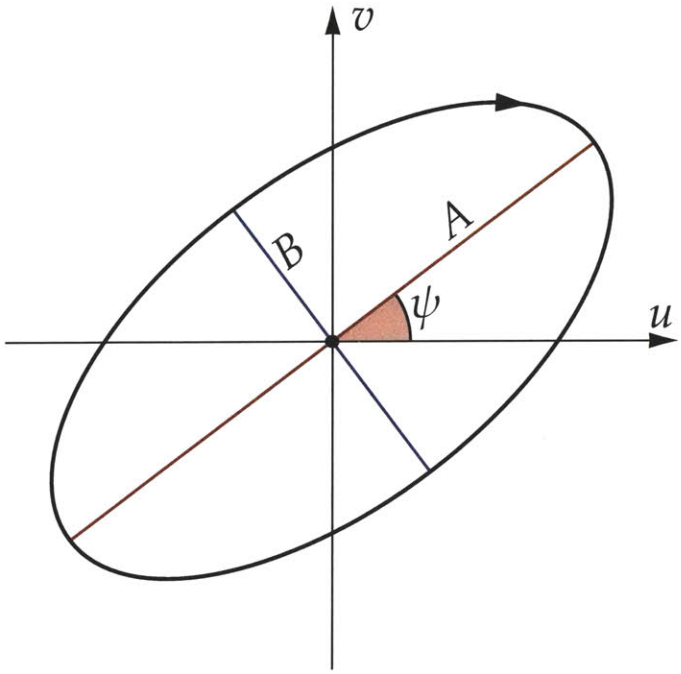

Figure 4-6: Conventions for quantifying radiation polarization in terms of an ellipse. ψ is the angle of the major axis, A is the magnitude of the major axis, and B is the magnitude of the orthogonal minor axis.

Ω.

Results

The complete set of polarization plots is too extensive to be included here, but the images can be found in Appendix A. Looking at major axis polarization angle (ψ) on the flat plate reflector (Figure A-1 and Figure A-3) we see the expected result: within the half power contour, ψ remains within about 2° of the look angle Ω. As the reflector rotates, the polarization of the system rotates by the same magnitude. In the case of the parabolic reflector (Figure A-2 and Figure A-4) we see extreme shifts in the fringe region, with polarization angles covering the entire range from 0° to 90°, but if we focus on the region inside the half power contour, we see much more promising results. ψ remains within about 2° of Ω, although now it shifts from left to right across the region. At the -10 dB contour the maximum difference between ψ and Ω reaches about 5°, which is worse than for the flat plate, but not significantly so. A polarization axis offset of 5° corresponds to less than half of a percent drop in gain ($\cos 5° \approx 0.996$) at worst, when the receiver is

perfectly linearly polarized.

Looking at eccentricity, on the flat plate (Figure A-5 and Figure A-7) we see a value of less than 0.1 out to both the $-3\,\mathrm{dB}$ and $-10\,\mathrm{dB}$ contours. The Ka-band configuration actually has a maximum value of 0.04. At 0.1 we really are only receiving 1% of the power in the minor axis direction since the power is proportional to the square of the field strength, so we can think of the receiver as almost completely linearly polarized. The parabolic configurations show significantly higher responses. In the Ka-band configuration (Figure A-8) we have a maximum eccentricity of 0.12 inside $-3\,\mathrm{dB}$ and 0.28 inside $-10\,\mathrm{dB}$. The value of 0.28 inside the $-10\,\mathrm{dB}$ ring corresponds to a gain of about 0.08 on the minor axis. Since it is in the low gain regions of the antenna pattern this is not a major factor, but the fact remains that the parabolic configuration causes the antenna system to be slightly elliptically polarized. At K-band (Figure A-6) the situation is worse, with a maximum eccentricity of 0.22 inside $-3\,\mathrm{dB}$ and 0.38 inside $-10\,\mathrm{dB}$. The factor of 0.38 corresponds to a power gain of 0.14 in the minor axis, and the value of 0.22 inside the half-power contour corresponds to 0.05. Looking at the total minor axis gain across the antenna we see a total power contribution of approximately 1% of the overall gain. This factor is not enormous, but certainly it is worth considering. As we would expect, the eccentricity does not change substantially as the reflector rotates. The visible changes that do take place are well outside the main beam of the antenna.

Chapter 5

Embedded Environmental Monitor

The voltage/temperature monitoring board, or embedded environmental monitor (EEM), is an original design for this project. It was first designed as a simple analog-to-digital converter (ADC) that could measure external voltages and external platinum resistance thermometers. The initial plan was to design the board with a PC/104 form factor and ISA bus interface and simply integrate the board into the flight computer PC/104 stack. This would incur a good deal of complexity in designing the board and writing the drivers for the flight computer, so a serial (RS-232) interface was chosen instead due to its simplicity. In addition, there was interest in producing a board with similar functionality for a nano-satellite (CubeSat) payload: the Micro-sized Microwave Atmospheric Sensor (MicroMAS). The board was designed to be as small as possible to be suitable for use in the satellite. Finally, as the development for MicroMAS progressed the board took on more responsibilities, including receiving instrument data from and controlling the radiometer, compressing the data, and encoding the data for transmission to the ground. The final housekeeping board will serve as a general purpose microcontroller with peripherals to measure voltages and bias and measure platinum resistance temperature devices (RTDs).

5.1 Hardware

The EEM incorporates a general purpose 16-bit microcontroller that operates at 16 MIPS. External digital peripherals include an Inter-Integrated Circuit (I2C) interface, as well as Serial Peripheral Interface (SPI) and Universal Asynchronous Receiver/Transmitter (UART) connections available over general purpose I/O pins. The EEM configuration for

NAST-M/K uses a single UART interface to communicate with a single board computer. For MicroMAS, a UART is used to talk to the satellite bus processor over an infrared (IrDA) link, a GPIO pin receives earth limb crossing information from a sensor, and SPI is used to receive data from the payload radiometer.

The EEM is powered off of two supply voltages, +5 V and +12 V, which were chosen based on what was available on both systems. The +5 V supply is regulated down to +3.3 V and +12 V down to +5 V. The two internal voltages are regulated using linear regulators in order to maximize isolation from the external supply voltages which are used in several places. Linear regulation is an inefficient way to produce the internal voltages, but produces much lower ripple than a switching supply without significant filtering. Even with inefficient regulation, the total power consumption of the board is very low, with the design calling for less than 100 mW average. In the MicroMAS configuration, most of this power is used by the microcontroller performing the ancillary processing tasks for the payload.

The analog sensors on the EEM include 12 three-wire inputs for RTDs, connected to ADCs with switchable current sources for biasing the RTDs. The three-wire configuration allows for compensation of probe wire resistance and thus significantly higher accuracy over the two-wire configuration without individual probe calibration. There is also an on-board analog output semiconductor temperature sensor connected to one of the ADC pins on the microcontroller. This sensor provides a simple ambient temperature measurement with no external connections. There are a total of four external inputs connected to resistor dividers for measuring external voltages. In addition, the four supply voltages present on the board itself are measured. These include the two external supply voltages at +5 V and +12 V as well as the internally regulated +5 V and +3.3 V supplies.

The on-board microcontroller is from the Microchip PIC24F series. The ADCs measuring the RTDs are Texas Instruments ADS1248 24-bit analog-to-digital converters with integrated current sources for biasing the RTDs. The analog temperature sensor is a Microchip MCP9700. The analog temperature sensor and the 8 measured voltages are read with the 10-bit ADC on the microcontroller, which can sample at a maximum rate of 500 ksps. The printed circuit board is 4 layers, chosen to allow for a smaller board and to incorporate internal power and ground planes for good signal isolation between the top and bottom routing layers. The digital and power connections to the board are standard

0.1 in (2.54 mm) single-row pin headers, and the higher pin count analog connections are 0.05 in (1.27 mm) double-row surface mount pin headers to keep the board size small. The outer dimensions for the board are 1.7 in (4.32 cm) square, with a total thickness of approximately 3 mm plus connectors. The EEM schematics and board layout are included in Appendix B.

The ADC for measuring voltages and the on-board temperature sensor operates at a maximum rate of 500 ksps. It can sample a single signal at a time. In practice we are not likely to be interested in sampling each signal more frequently than about 1 Hz, so the ADC is easily able to accomplish this. The RTD ADCs are significantly slower since they are designed for precision rather than as a general purpose product. Each ADC can sample one of its eight channels (corresponding to four temperature probes) at a rate of 2 ksps. Again, we are likely only interested in measuring the sensors at a rate of perhaps 1 Hz, so the converters are more than adequate.

The RTD probes are structured as a three wire element. This design allows us to remove the resistance of the wires when measuring the resistance across the sensor. This can be a significant factor when we are looking for a very small resistance change. All three of the probe wires are identical. Two of the wires are joined at one side of the resistance element, and the other wire is attached to the other side. One of the wires in the pair is the return, and the other wire in the pair and the third wire on the other side of the element are connected to the ADC inputs. The temperature ADCs have a precision current source which can be fed out any of the ADC inputs, and the ADC can simultaneously sense the voltage at this input. In this way, the ADC effectively measures the resistance of the two inputs.

The temperature is measured in two steps. The first step consists of a current traveling through the pair of wires on one side of the sensor element, and not passing through the element. This measures the resistance of two probe wires. The second input has the current travel down the third wire, through the element, and back through the return wire. Since we are using a current source, the voltage drop across the wires is the same, and we can find the voltage drop across the probe by subtracting the second measurement from the first. This voltage gives us the resistance of the probe, which has been calibrated to have a very specific temperature to resistance relationship.

5.2 Software

When operating solely as an environmental monitor, the board starts up and configures the necessary peripherals. These include the on-board ADC, the three SPI interfaces for the temperature ADCs, and the serial interface (UART) to communicate with the flight computer. Since the only purpose of this board is to monitor sensors, it will not accept commands from the flight computer, but will simply send out a string of sensor values once per second. Once the peripherals are configured, the microcontroller enters the main loop, which samples each ADC input, and sends commands to the three temperature ADCs to bias each of their eight channels and perform a measurement. Two channels correspond to each temperature sensor, and the difference between the measured values is the parameter of interest. These peripherals are operated using separate interrupts to avoid waiting for a given peripheral. This is unnecessary in NAST-K, but when the board is performing more processing tasks it needs to have as much time available as possible. Once all the sensors are measured the raw counts recorded are packaged into a data packet and sent over to the flight computer for logging. The computer will log the measurement time along with the data. The board does no calculation on the counts to find a real temperature—this will be performed off-line based on the board calibration data from testing.

When operating in the configuration for MicroMAS, the board must assume several additional responsibilities. The same interrupt-driven data collection will take place, although perhaps at a reduced rate if necessary. Instead of idling in the main loop, the board will spend most of the time applying compression and adding error correction information to the data from the payload radiometer as well as the voltage and temperature data. The board is also responsible for monitoring the earth limb sensor, which it will do by interrupting on the earth limb crossing signal and starting a timer to determine how far in the past the crossing occurred. This timer count will be sent to the satellite bus along with the payload and environmental data. The satellite bus will subtract the count from the current time to determine when the limb crossing occurred, and feed this information into its guidance control system. Since it is currently undetermined whether or not there will be a continuous communication link between the payload and the satellite bus, the EEM must buffer at least one satellite rotation worth of data for burst transmis-

sion at the right moment. The EEM will receive a signal from the satellite bus when it is ready to transmit, and the payload will then send the data over.

Chapter 6

Conclusions

6.1 System design

The overall system design was fairly straightforward, but left several areas for design improvements. We found a stepper motor with enough torque to directly drive the reflector. This was useful because it allowed us to design the system with no gearbox which provided two advantages: first, we had limited room on the back side of the instrument, at the location of the motor due to requirements from the aircraft manufacturer, and second, the lack of a gearbox significantly reduces the backlash in the system. The flight computer software design should be very robust to failure, fixing an issue found in NAST-M where the operating system would periodically be corrupted or exhibit erroneous behavior requiring that the flash disk be replaced. Replacing the camera system significantly helped finding space for the payload in the aircraft. Removing the rack unit associated with the camera frame-grabber and computer provides valuable room in the equipment rack for the new flight computer.

6.2 Antenna system

The design of the horn and reflector system yielded a very inexpensive option for designing an instrument capable of receiving two fairly separated bands (with $\Delta\nu/\nu \approx 0.32$). The alternative would have been to build two independent radiometers with two separate feeds. This would allow for matched beamwidths, but the two feeds could not be located at the same point. This is not a concern with a flat reflector, but a flat reflector would

not provide the tight beam patterns consistent with NAST-M. With a parabolic, having a feed not located at the focal point of the reflector will degrade performance considerably. With the diameter of the reflector in NAST-K on the same scale as the focal length and the horn size, the offset from focal length introduced by two horns may have required two parabolic reflectors.

Since the design uses a single feed, one problem with using the flat plate, in addition to the wide beamwidth, is the fact that the two frequency bands will not be matched in beamwidth. The parabolic reflector solves this problem, because the single feed will illuminate the parabolic reflector differently at each band, and thus the effective size of the reflector will be proportional to that of the horn beamwidth. This effect allows us to very closely match the beamwidths between the two bands. We have found that the parabolic reflector does have a negative impact on the receiver polarization, but that this effect is small and largely effects the sidelobes of the antenna. Finally, at these frequencies the tolerance required on the surface of a parabolic reflector is very reasonable. Since the parabolic shape can be easily programmed into a standard computer-controlled milling machine, the fabrication costs of a parabolic reflector are not significantly more than that of a flat plate, and they are certainly much lower than that of a corrugated scalar feed horn.

6.3 Embedded environmental monitor

The embedded environmental monitor board was an interesting design, because it was expected to operate with two separate payloads using different digital interfaces, and to perform different processing functions on each payload. A lot of work went into making the board as small as possible, and this seems to have paid off, with the fine-pitch external connectors ending up as the biggest limiting factor for board size. Although the satellite integration of the board is currently only intended for the engineering bench model, it will be interesting to see how well the design fares in such a resource constrained environment.

6.4 Future work

Moving forward, a lot of testing and system integration work will take place with NAST-K. When the radiometer is received from the vendor its performance will be verified, and then it can be integrated into the mechanical assembly. Many of the components of the instrument have been assembled, including the camera, flight computer, video amplifiers, and the EEM board, but others need to be fabricated. Once the components have been acquired, mechanical and electrical integration will take place at Lincoln Laboratory, and we will continue working with the aircraft team to prepare the wing-pod for the new instrument. The NPP satellite is slated to be launched in late October 2011, so the tentative goal is to have the instrument ready for an initial flight campaign soon after this time.

6.5 Conclusions

Once completed, NAST-K will be a useful tool in the operational validation process for NPP after launch and for future NPOESS satellites. NAST-M and NAST-K will be capable of receiving all of the ATMS channels associated with weather products below the flight altitude of the sensor, meaning that they should be able to produce corroborated data for all of the channels reasonably measured with an airborne platform. NAST-K will also be useful in future science missions requiring surface microwave measurements with significantly higher resolution than what is available in the operational satellite platforms. With an effective spot area over 1000 times smaller than ATMS, NAST-K can provide an entirely different view of the surface.

Appendix A

Antenna Polarization Patterns

This appendix contains plots of antenna elliptical polarization parameters versus reflector look angle for the flat plate and parabolic reflectors. These parameters, which were calculated as described in Section 4.3.4, are elliptical major axis polarization angle (ψ), polarization eccentricity (B/A), major axis gain (A^2 in dBi), and minor axis gain (B^2 in dBi). The plots are displayed for reflector look angles Ω of 0°, 15°, 30°, 45°, 60°, and 90°.

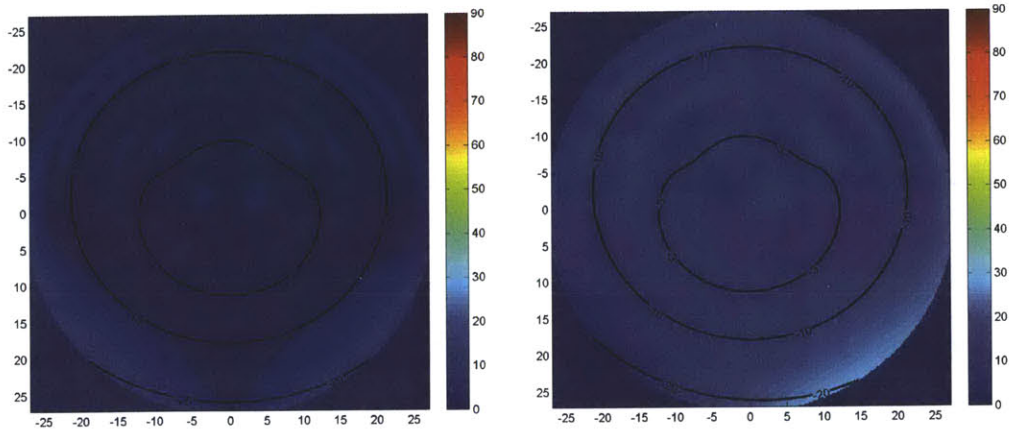

(a) $\Omega = 0°$

(b) $\Omega = 15°$

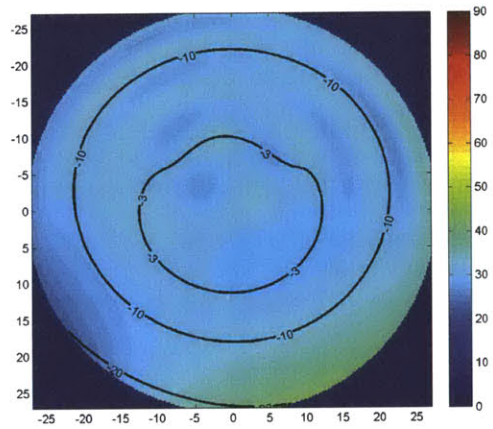

(c) $\Omega = 30°$

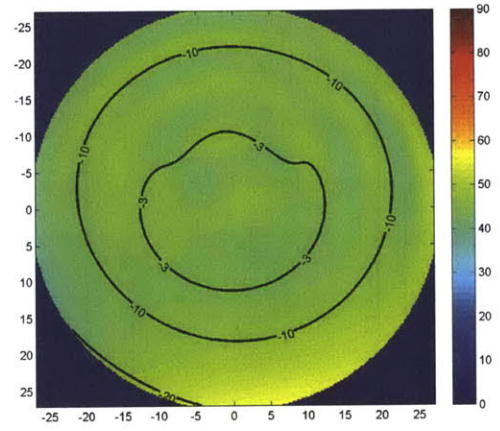

(d) $\Omega = 45°$

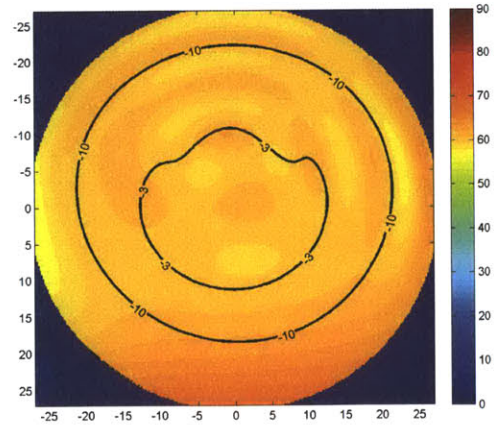

(e) $\Omega = 60°$

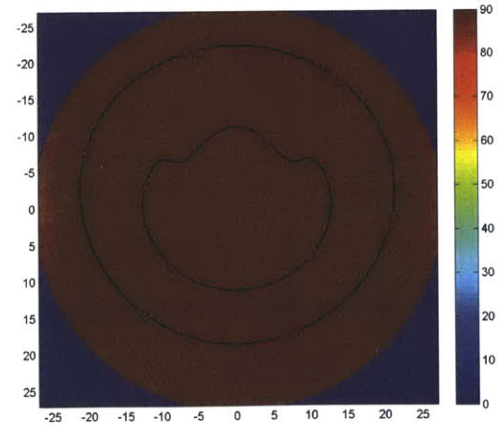

(f) $\Omega = 90°$

Figure A-1: Major axis polarization angle (ψ) versus look angle (Ω) for the K-band flat plate reflector. Plots are centered at boresight, and the coordinates are polar as described in Section 4.2.1 with the distance from the center representing θ and the rotation angle ϕ. Overlaid on the plot are contours for total gain at -3, -10, -20, and -30 dB below peak.

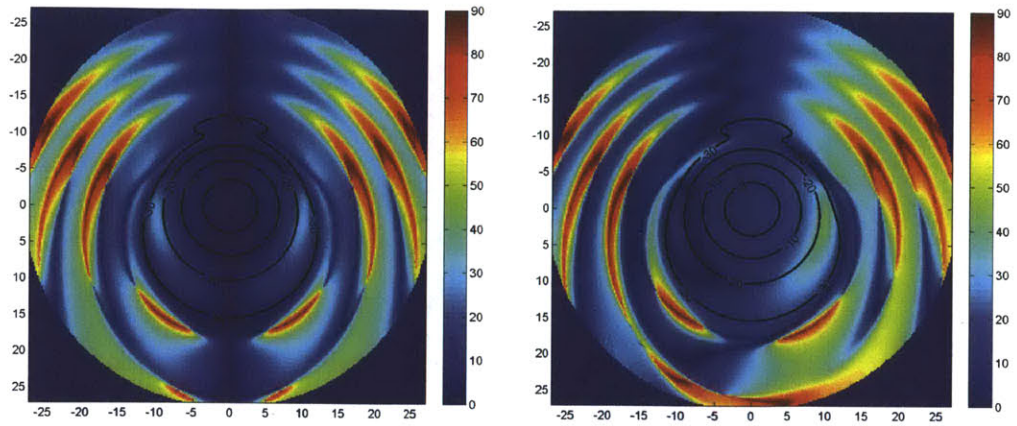

(a) $\Omega = 0°$

(b) $\Omega = 15°$

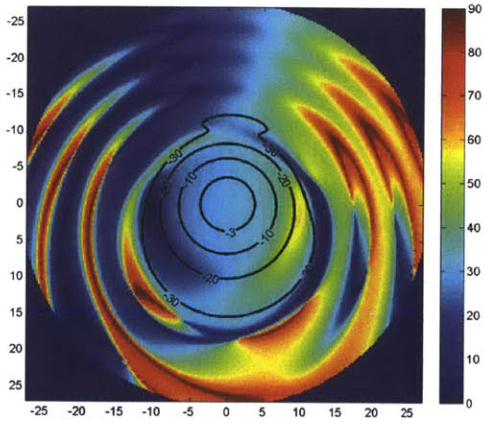

(c) $\Omega = 30°$

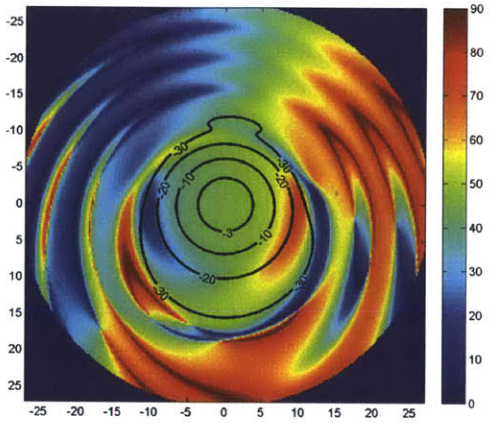

(d) $\Omega = 45°$

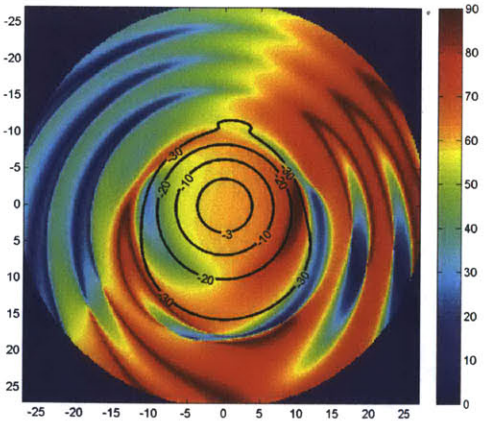

(e) $\Omega = 60°$

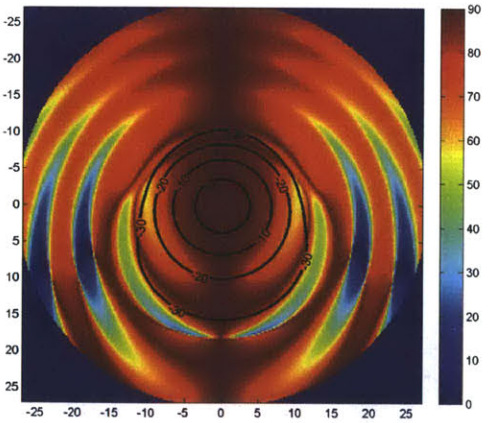

(f) $\Omega = 90°$

Figure A-2: Major axis polarization angle (ψ) versus look angle (Ω) for the K-band parabolic reflector. Plots are centered at boresight, and the coordinates are polar as described in Section 4.2.1 with the distance from the center representing θ and the rotation angle ϕ. Overlaid on the plot are contours for total gain at -3, -10, -20, and -30 dB below peak.

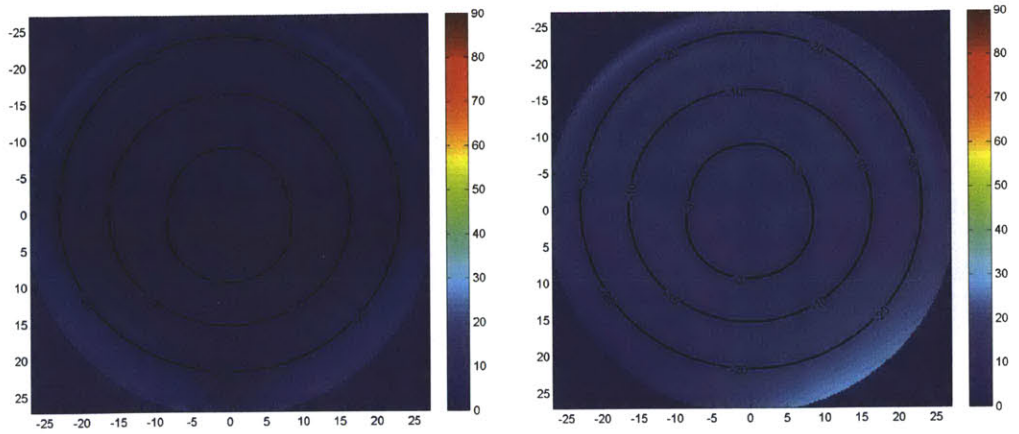

(a) $\Omega = 0°$

(b) $\Omega = 15°$

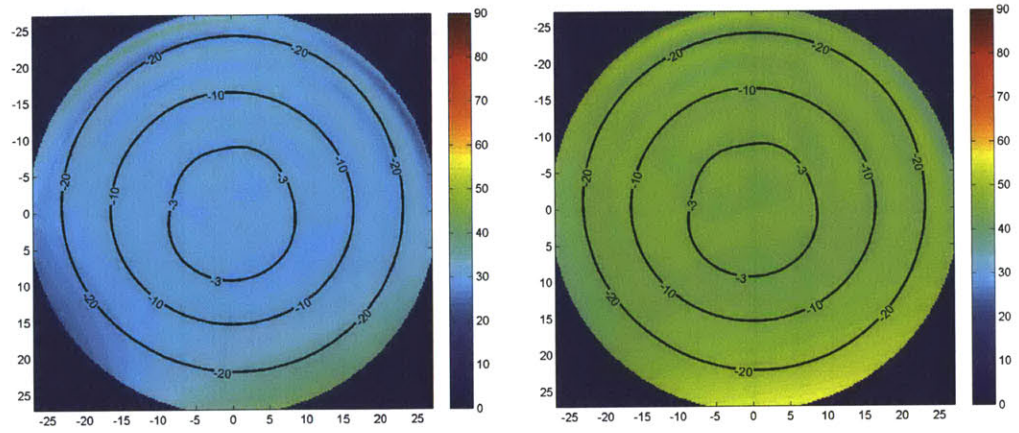

(c) $\Omega = 30°$

(d) $\Omega = 45°$

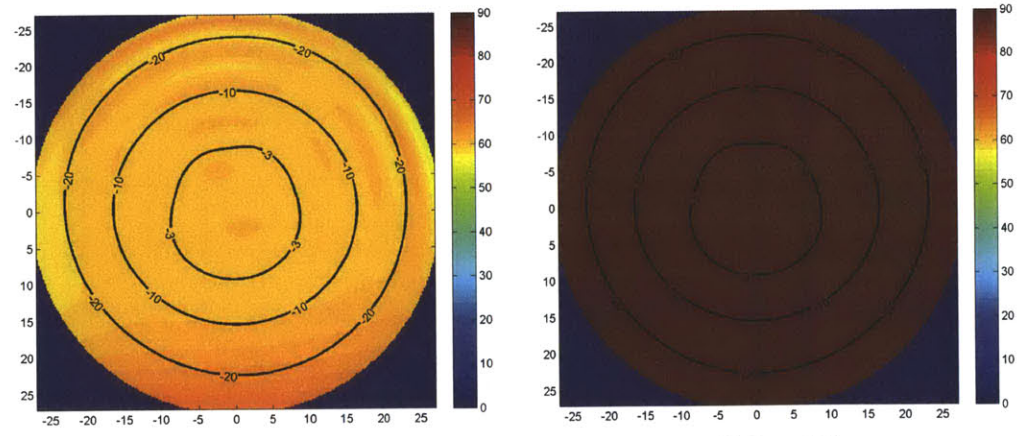

(e) $\Omega = 60°$

(f) $\Omega = 90°$

Figure A-3: Major axis polarization angle (ψ) versus look angle (Ω) for the Ka-band flat plate reflector. Plots are centered at boresight, and the coordinates are polar as described in Section 4.2.1 with the distance from the center representing θ and the rotation angle ϕ. Overlaid on the plot are contours for total gain at -3, -10, -20, and -30 dB below peak.

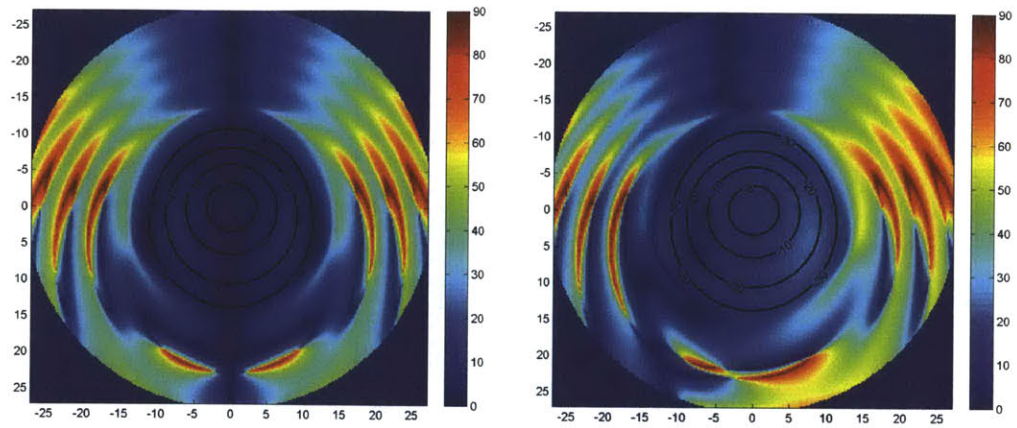

(a) $\Omega = 0°$

(b) $\Omega = 15°$

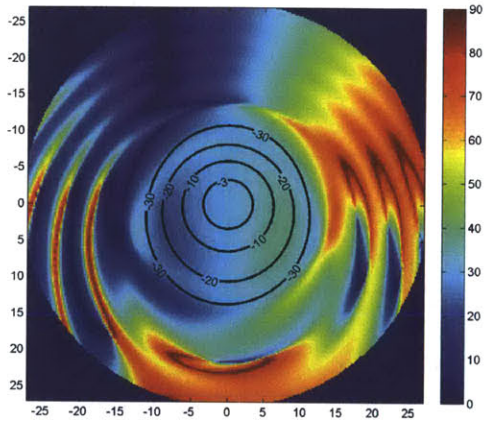

(c) $\Omega = 30°$

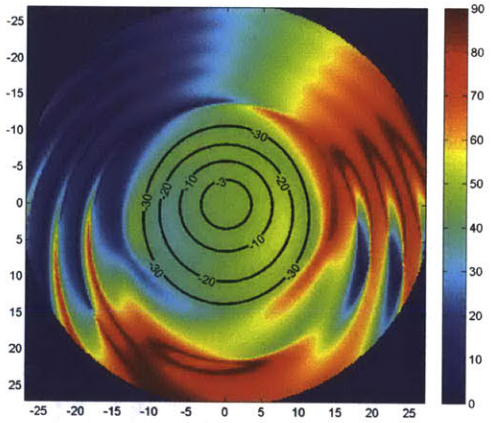

(d) $\Omega = 45°$

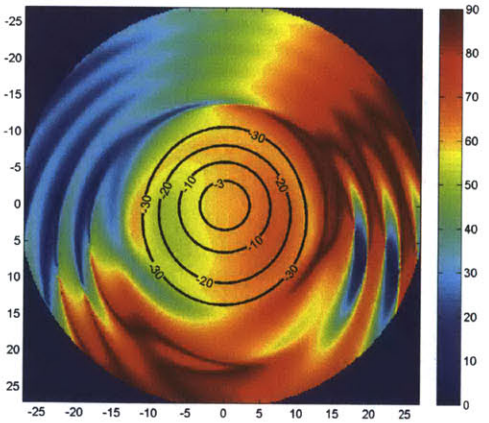

(e) $\Omega = 60°$

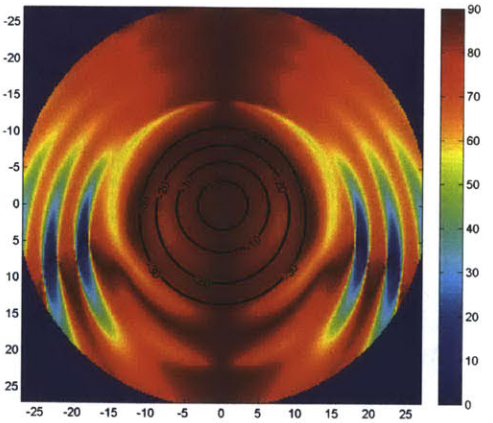

(f) $\Omega = 90°$

Figure A-4: Major axis polarization angle (ψ) versus look angle (Ω) for the Ka-band parabolic reflector. Plots are centered at boresight, and the coordinates are polar as described in Section 4.2.1 with the distance from the center representing θ and the rotation angle ϕ. Overlaid on the plot are contours for total gain at -3, -10, -20, and -30 dB below peak.

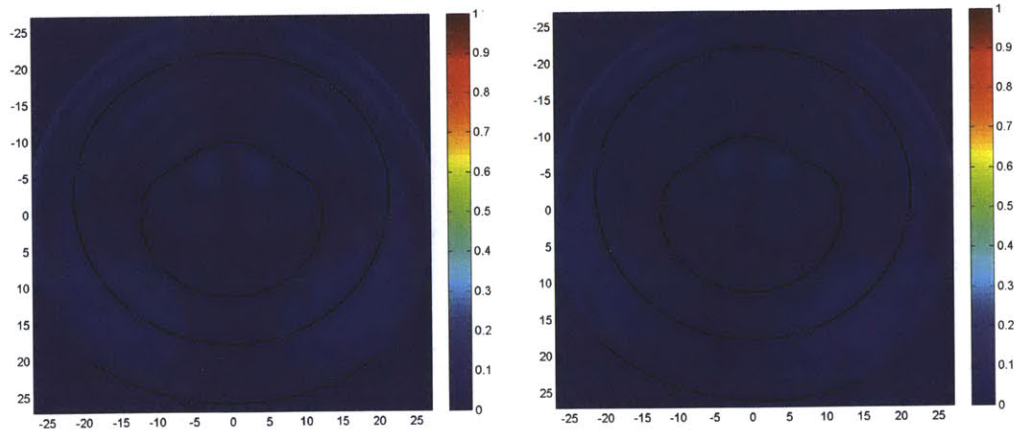

(a) $\Omega = 0°$

(b) $\Omega = 15°$

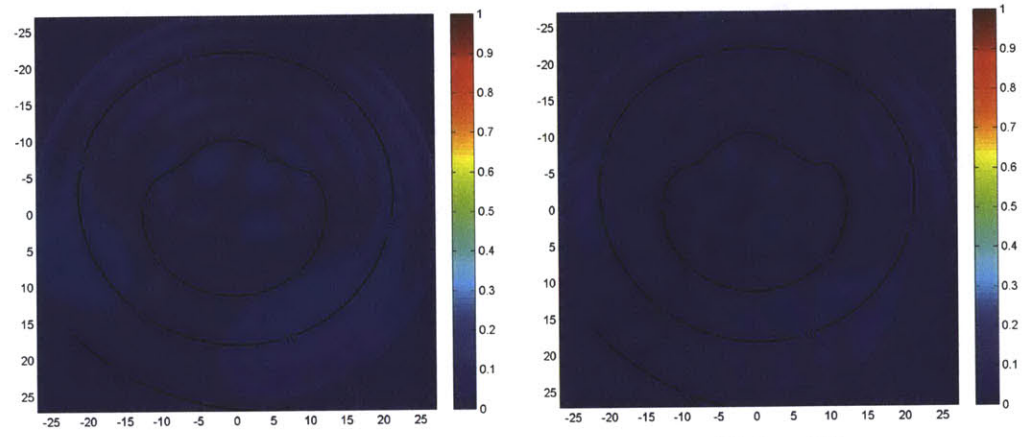

(c) $\Omega = 30°$

(d) $\Omega = 45°$

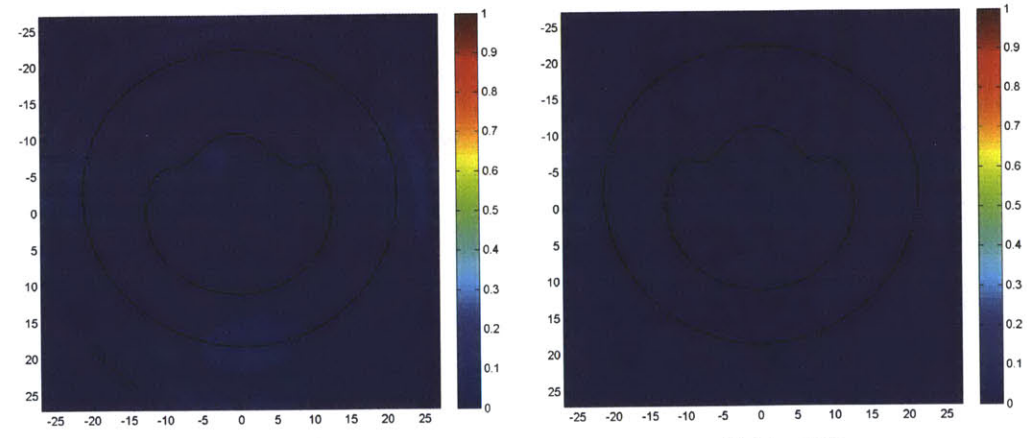

(e) $\Omega = 60°$

(f) $\Omega = 90°$

Figure A-5: Elliptical eccentricity (B/A) versus look angle (Ω) for the K-band flat plate reflector. Plots are centered at boresight, and the coordinates are polar as described in Section 4.2.1 with the distance from the center representing θ and the rotation angle ϕ. Overlaid on the plot are contours for total gain at -3, -10, -20, and -30 dB below peak.

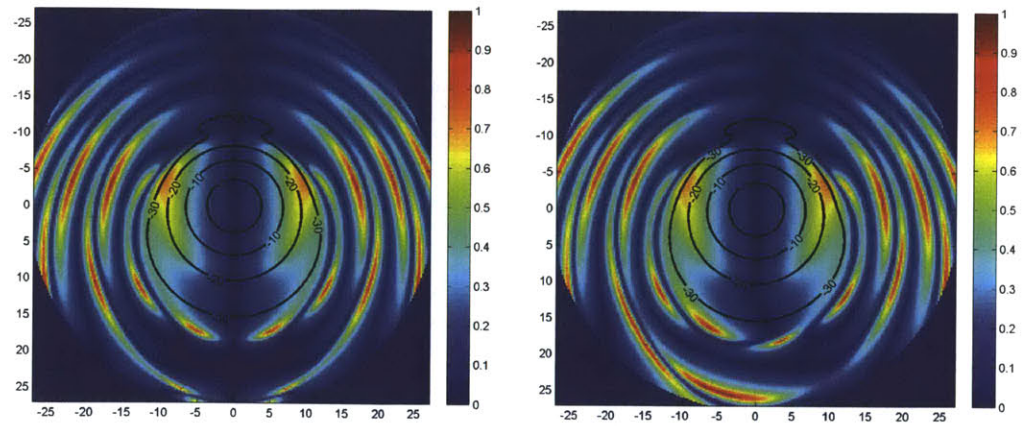

(a) $\Omega = 0°$

(b) $\Omega = 15°$

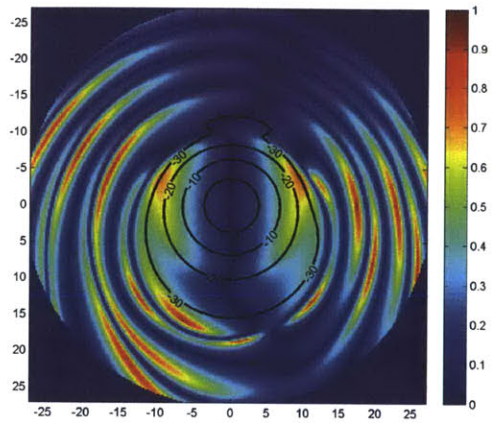

(c) $\Omega = 30°$

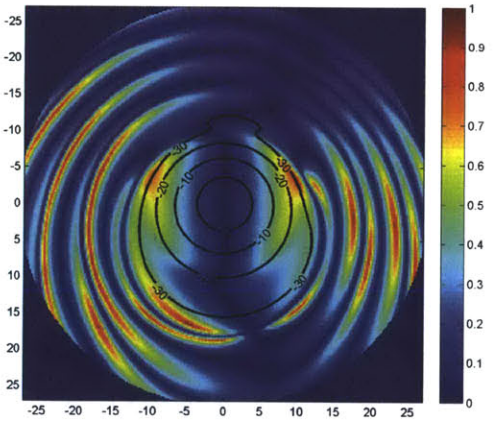

(d) $\Omega = 45°$

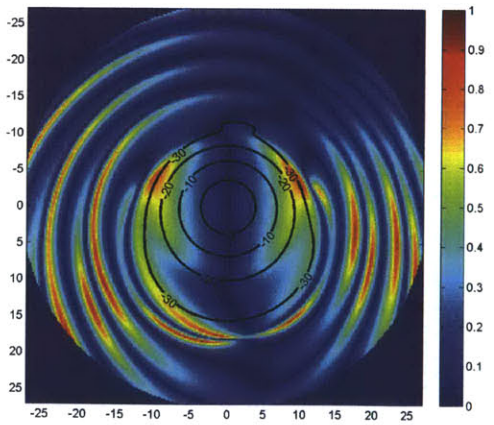

(e) $\Omega = 60°$

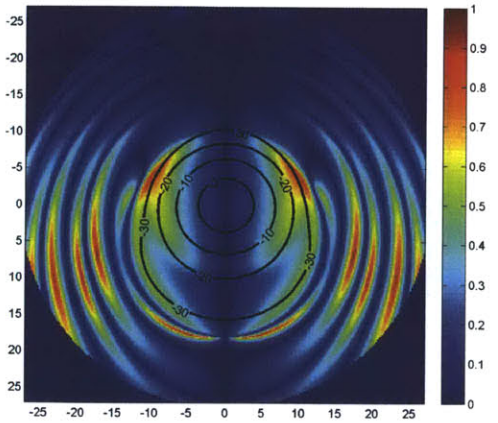

(f) $\Omega = 90°$

Figure A-6: Elliptical eccentricity (B/A) versus look angle (Ω) for the K-band parabolic reflector. Plots are centered at boresight, and the coordinates are polar as described in Section 4.2.1 with the distance from the center representing θ and the rotation angle ϕ. Overlaid on the plot are contours for total gain at -3, -10, -20, and -30 dB below peak.

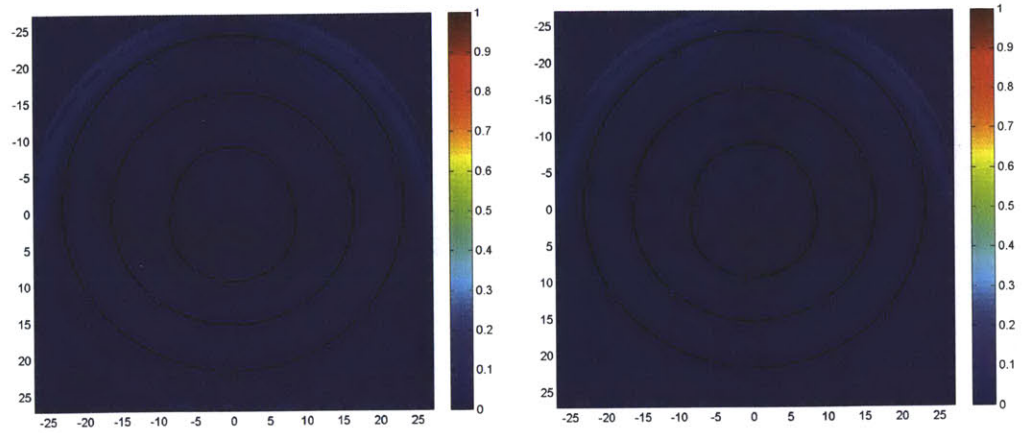

(a) $\Omega = 0°$

(b) $\Omega = 15°$

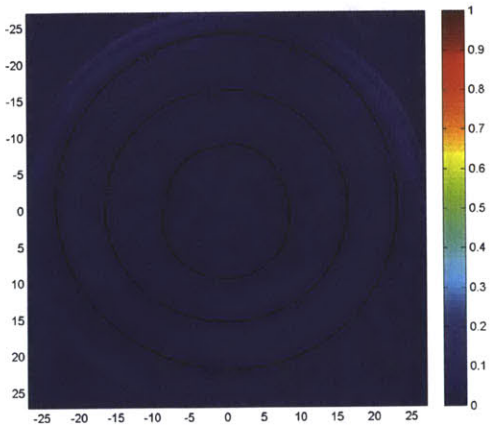

(c) $\Omega = 30°$

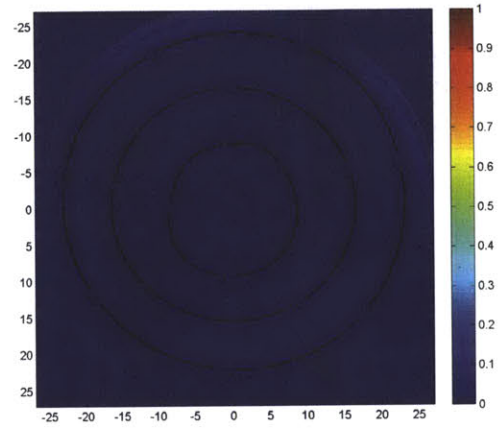

(d) $\Omega = 45°$

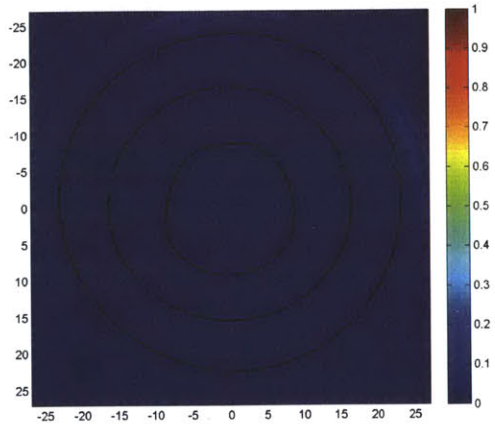

(e) $\Omega = 60°$

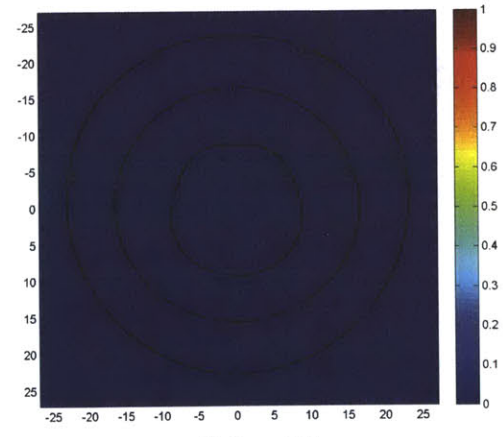

(f) $\Omega = 90°$

Figure A-7: Elliptical eccentricity (B/A) versus look angle (Ω) for the Ka-band flat plate reflector. Plots are centered at boresight, and the coordinates are polar as described in Section 4.2.1 with the distance from the center representing θ and the rotation angle ϕ. Overlaid on the plot are contours for total gain at -3, -10, -20, and -30 dB below peak.

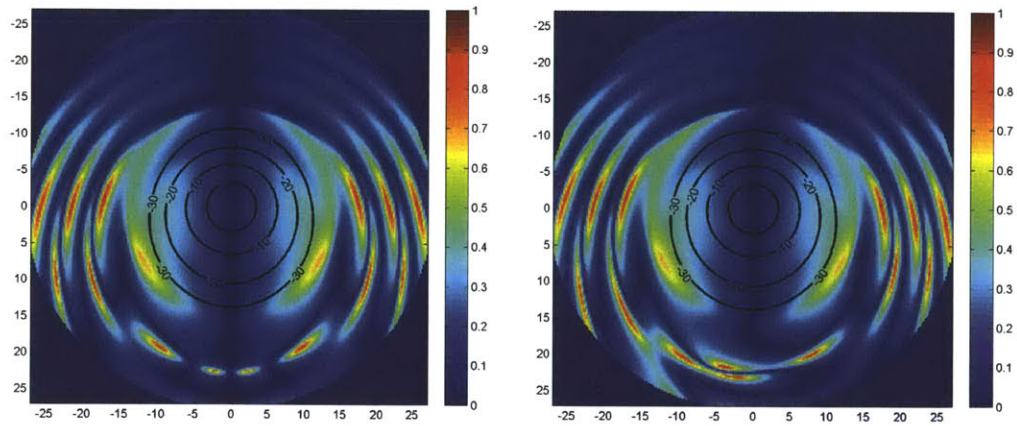

(a) $\Omega = 0°$

(b) $\Omega = 15°$

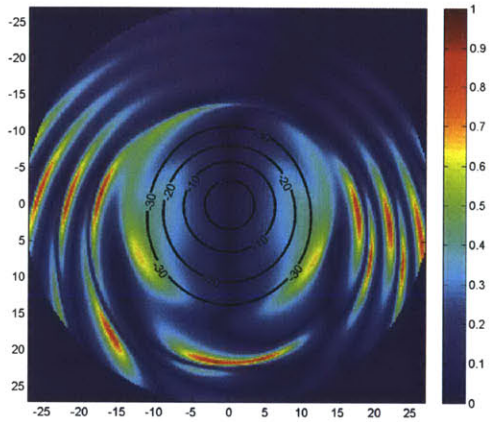

(c) $\Omega = 30°$

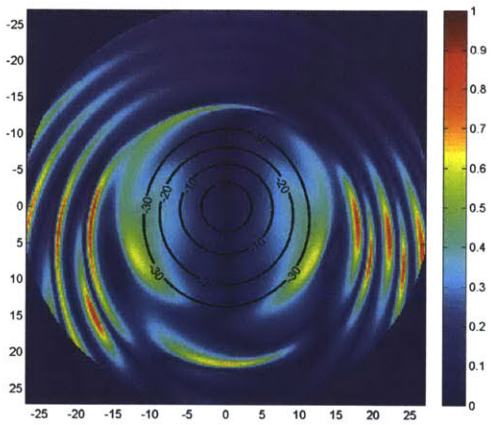

(d) $\Omega = 45°$

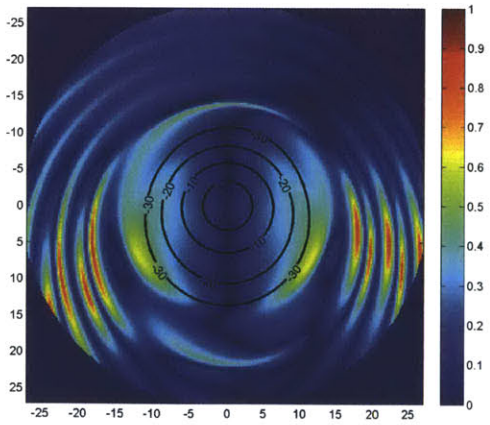

(e) $\Omega = 60°$

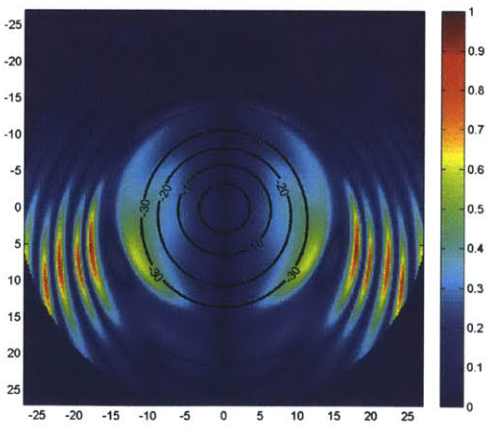

(f) $\Omega = 90°$

Figure A-8: Elliptical eccentricity (B/A) versus look angle (Ω) for the Ka-band parabolic reflector. Plots are centered at boresight, and the coordinates are polar as described in Section 4.2.1 with the distance from the center representing θ and the rotation angle ϕ. Overlaid on the plot are contours for total gain at -3, -10, -20, and -30 dB below peak.

Appendix B

PCB Schematics and Layouts

This appendix includes the schematics and PCB layouts for the two original circuits designed for this work: the receiver video amplifier and the embedded environmental monitor. The video amplifier is described in Section 3.4, and the embedded environmental monitor is covered in Chapter 5.

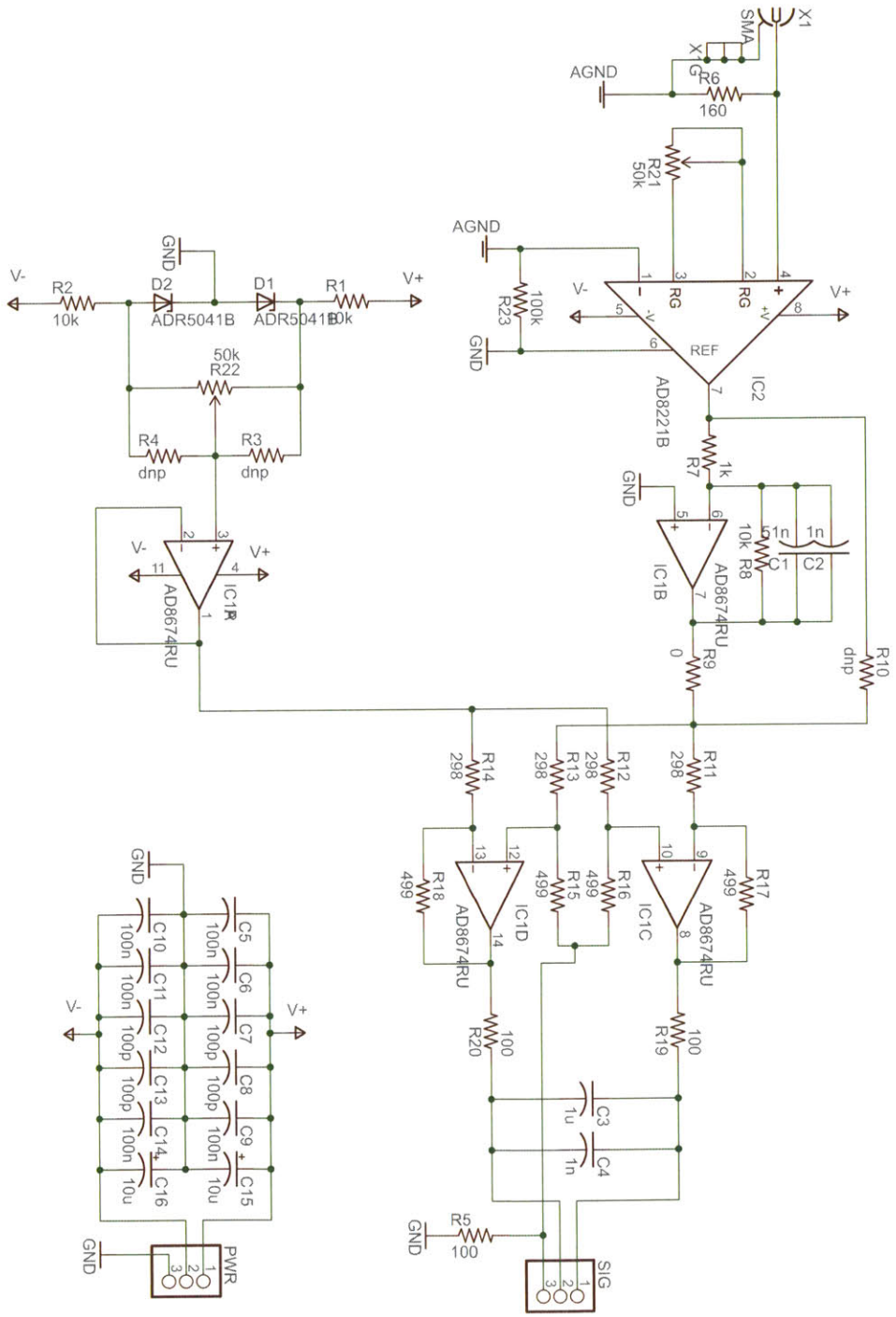

Figure B-1: Video amplifier schematic

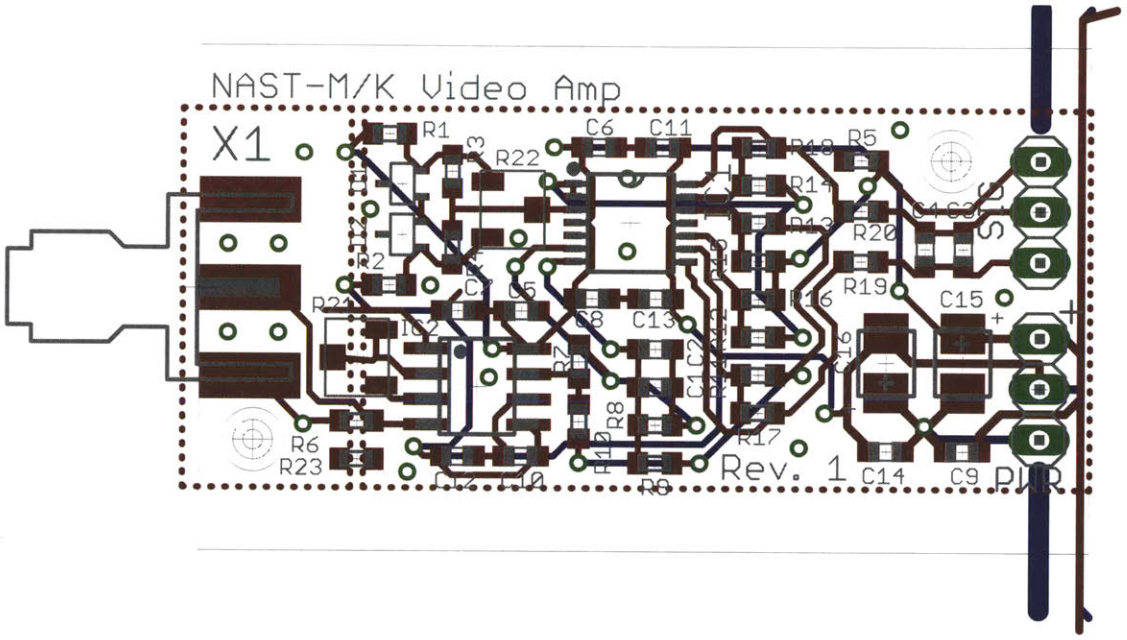

Figure B-2: Video amplifier PCB layout. The thin grey line is the board outline, and the traces extending off the board at the top and bottom show the bussed power connections between adjacent boards when they are attached. The thick dotted regions represent ground polygon fills on the top and bottom board layers.

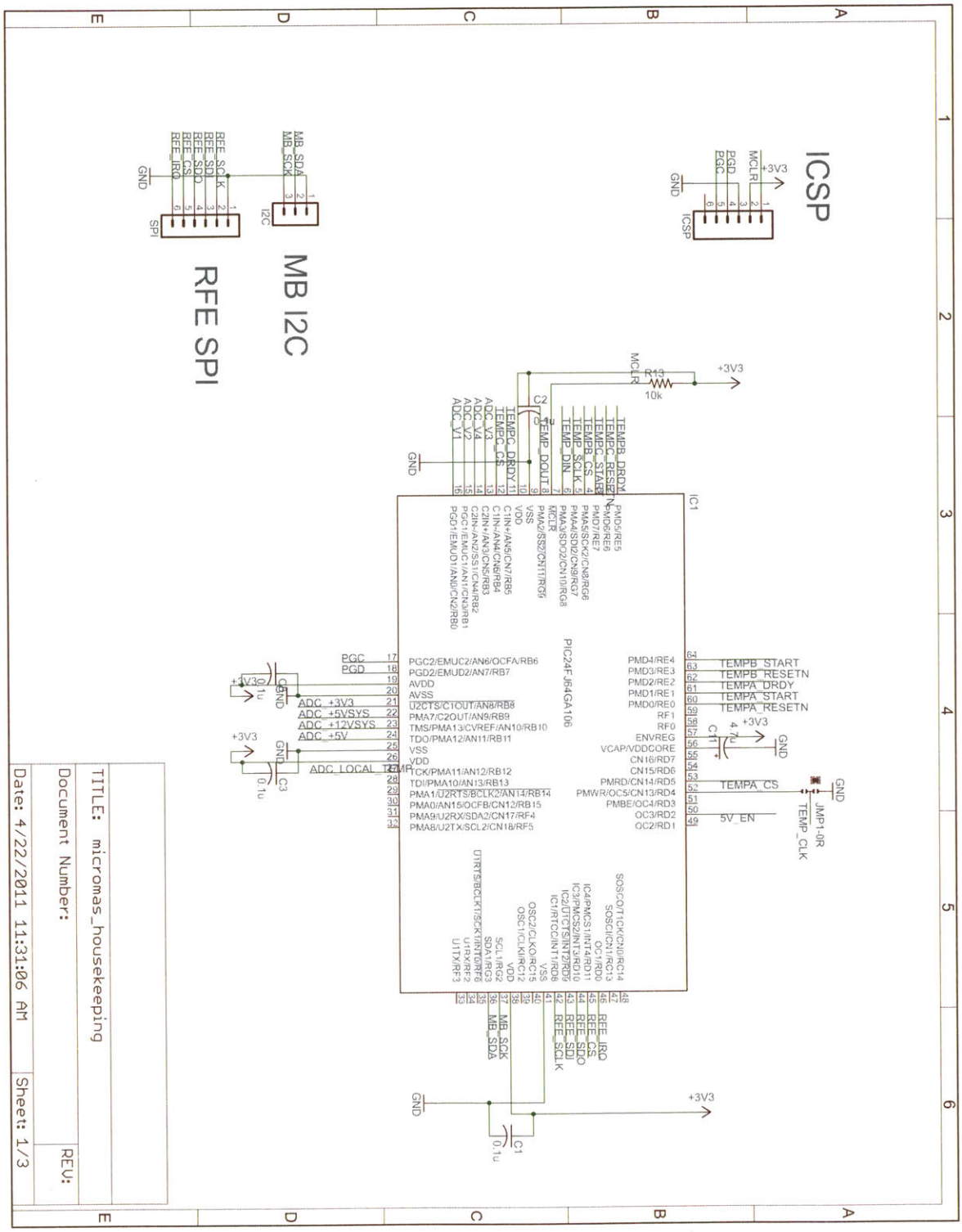

Figure B-3: Embedded environmental monitor schematic (1/3) showing the microcontroller and digital interfaces.

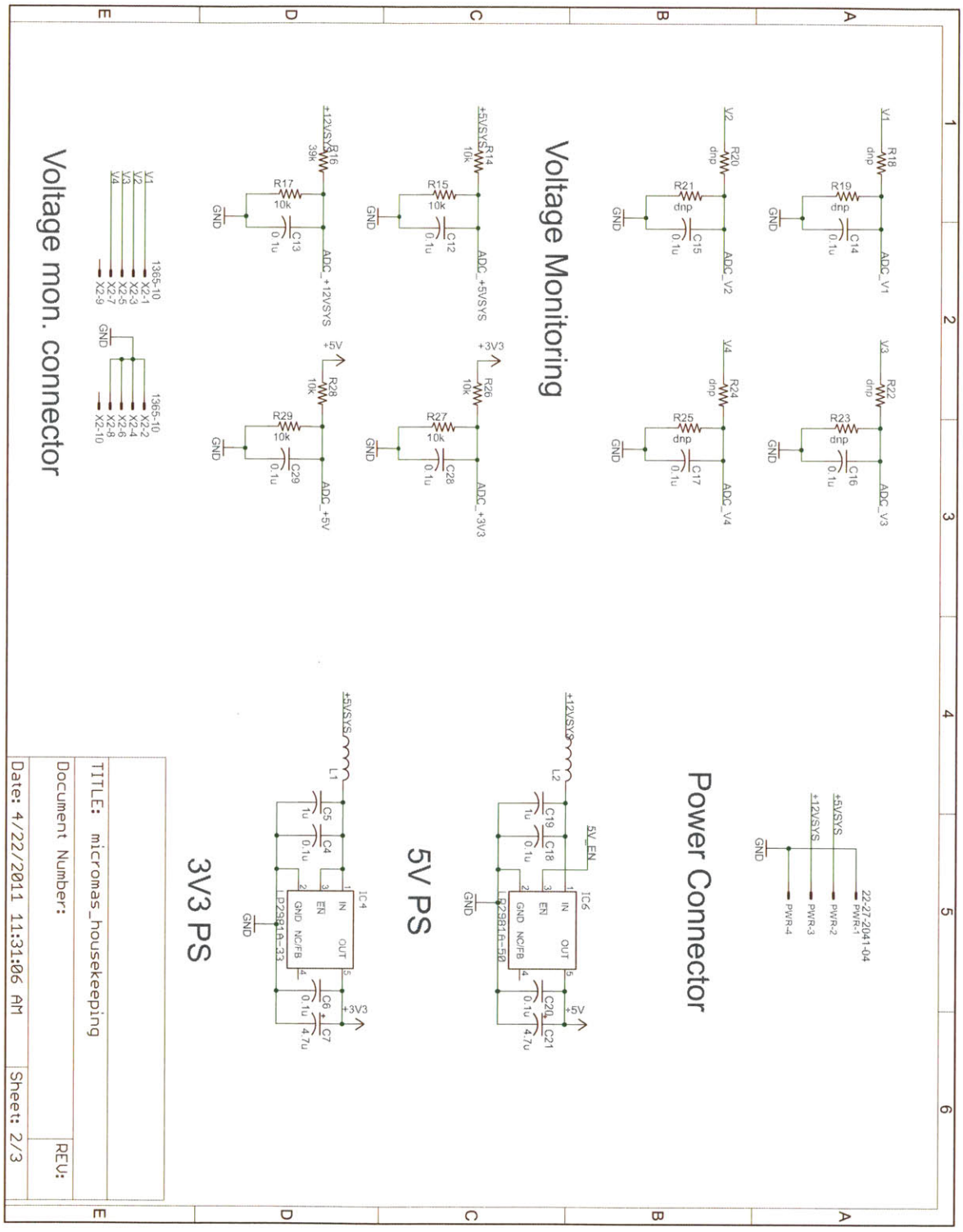

Figure B-4: Embedded environmental monitor schematic (2/3) showing the power supply and analog voltage input dividers.

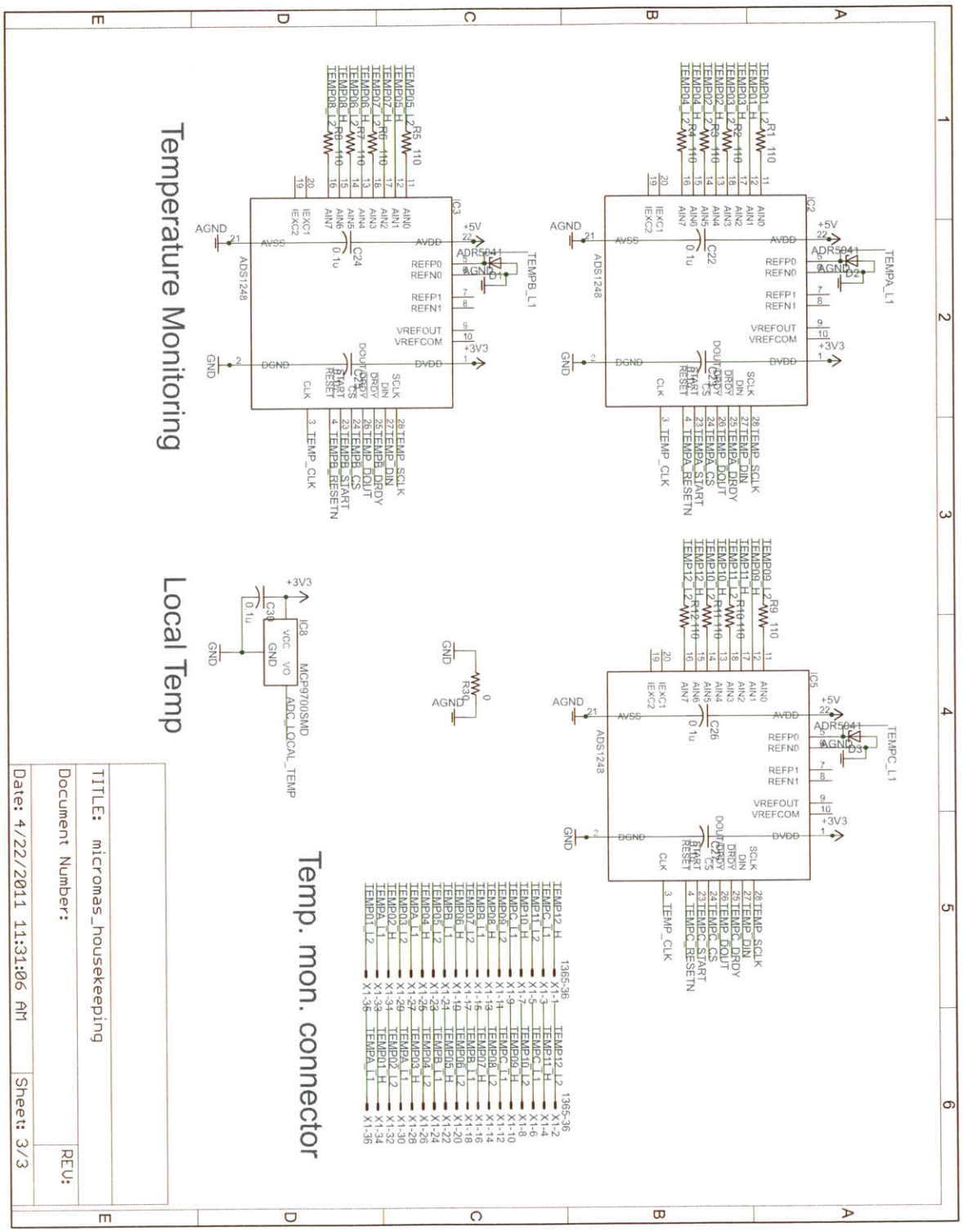

Figure B-5: Embedded environmental monitor schematic (3/3) showing the temperature measurement circuits and external analog connectors.

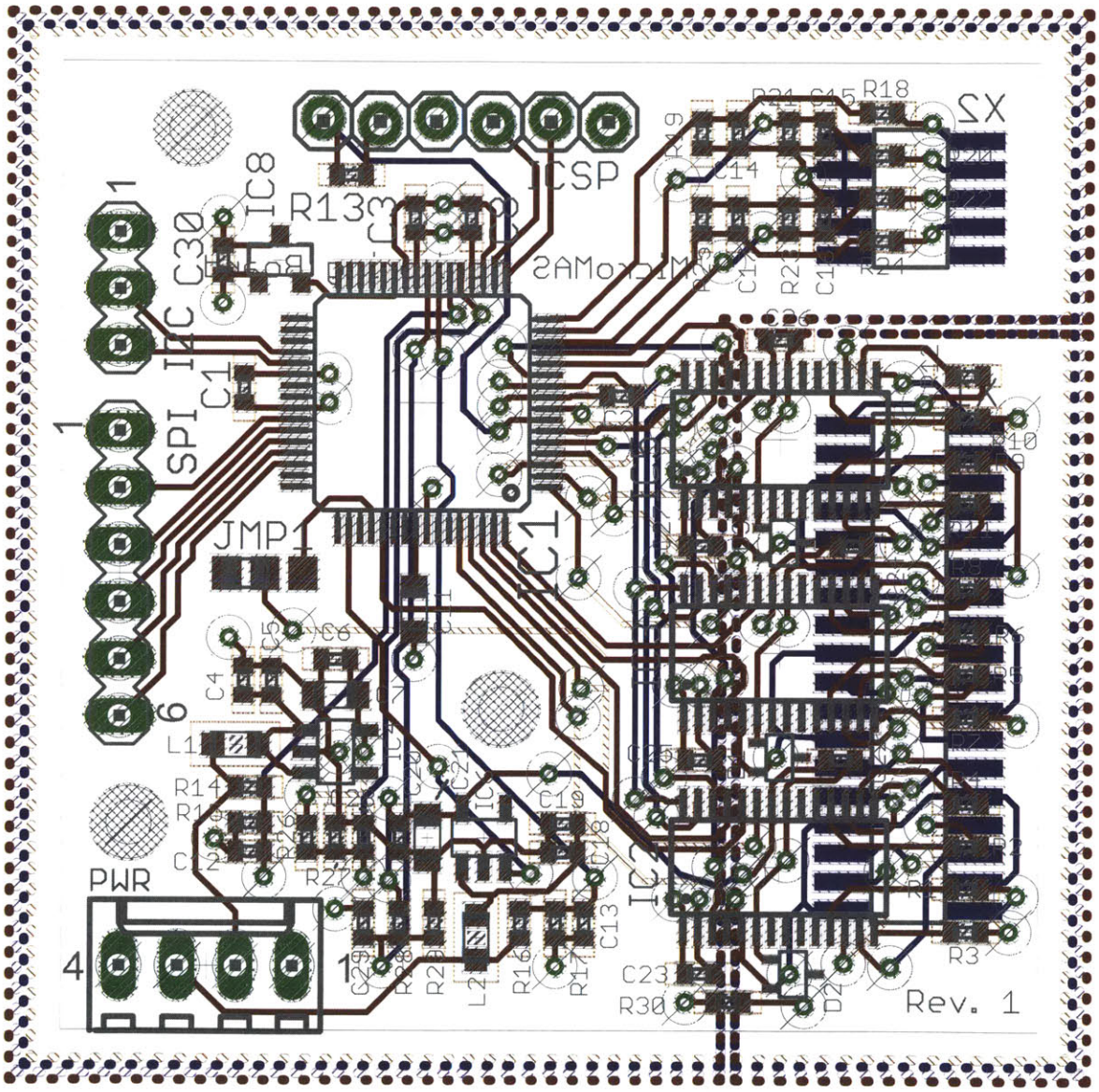

Figure B-6: Embedded environmental monitor PCB layout. The thin grey line is the board outline, and the thick dotted regions are power and ground polygon fills on all four layers.

Bibliography

[1] W. Blackwell, J. Barrett, F. Chen, R. Leslie, P. Rosenkranz, M. Schwartz, and D. Staelin. NPOESS Aircraft Sounder Testbed-Microwave (NAST-M): Instrument description and initial flight results. *Geoscience and Remote Sensing, IEEE Transactions on*, 39(11):2444–2453, 2001.

[2] W. Blackwell and D. Staelin. Comparative performance analyses of passive microwave systems for tropospheric sounding of temperature and water vapor profiles. In *Proceedings of SPIE*, volume 2812, page 472, 1996.

[3] W. J. Blackwell. *Retrieval of cloud-cleared atmospheric temperature profiles from hyperspectral infrared and microwave observations*. Sc.D. thesis, Massachusetts Institute of Technology, 2002.

[4] L. Blake and M. Long. *Antennas: fundamentals, design, measurement*. SciTech Pub., 2009.

[5] C. Brann. Status and activities of the NPOESS Advanced Technology Microwave Sounder (ATMS) in preparation for delivery to the NPOESS spacecraft. In *Fifth Annual Symposium on Future Operational Environmental Satellite Systems-NPOESS and GOES-R*, 2009.

[6] R. Bucknam. *NAST-M/K 3D Mechanical Model*. MIT Lincoln Laboratory, 2011.

[7] E. Chuvieco and A. Huete. *Fundamentals of Satellite Remote Sensing*. Taylor & Francis, 2009.

[8] Diamond Systems, Inc. Helios PC/104 single board computer. `http://www.diamondsystems.com/products/helios`.

[9] M. Klein. *Proposal: K-band and Ka-band Radiometer*. Boulder Environmental Sciences and Technology, 2010.

[10] R. Leslie and D. Staelin. NPOESS aircraft sounder testbed-microwave: observations of clouds and precipitation at 54, 118, 183, and 425 GHz. *Geoscience and Remote Sensing, IEEE Transactions on*, 42(10):2240–2247, 2004.

[11] R. V. Leslie. *Geophysical parameter estimation with a passive microwave spectrometer at 54 / 118 / 183 / 425 GHz*. Sc.D. thesis, Massachusetts Institute of Technology, 2004.

[12] J. A. Martinez-Lorenzo. Reflector antenna for a K-band and Ka-band radiometer. 2010.

[13] M. Mishchenko, L. Travis, and A. Lacis. *Multiple scattering of light by particles: radiative transfer and coherent backscattering*. Cambridge University Press, 2006.

[14] C. Muth, P. Lee, J. Shiue, A. Webb, et al. Advanced technology microwave sounder on NPOESS and NPP. In *Geoscience and Remote Sensing Symposium, 2004. IGARSS'04. Proceedings. 2004 IEEE International*, volume 4, pages 2454–2458. IEEE, 2004.

[15] National Aeronautics and Space Administration. GOES POES program - POES instruments. `http://goespoes.gsfc.nasa.gov/poes/instruments/index.html`.

[16] National Aeronautics and Space Administration, Dryden Flight Research Center, Edwards, CA 93523-0273. *ER-2 Airborne Laboratory Experimenter Handbook*, August 2002.

[17] NOAA and USAF. US standard atmosphere, 1976. *US Government Printing Office, Washington, DC*, 1976.

[18] NOAA National Environmental Satellite Data and Information Service (NESDIS). NPP ATMS product suite: Microwave integrated retrieval system algorithms. `http://www.star.nesdis.noaa.gov/smcd/spb/mirs/product.html`.

[19] Y. Rahmat-Samii, R. A. Hoferer, and H. Mosallaei. Beam efficiency of reflector antennas: The simple formula. *IEEE Antennas and Propogation Magazine*, 40(5):82–87, 1998.

[20] P. Rosenkranz. Absorption of microwaves by atmospheric gases. In *Atmospheric remote sensing by microwave radiometry*, volume 1, page 37, 1993.

[21] M. Scarito. *K-/Ka-band Radiometer Specification*. MIT Lincoln Laboratory, 2010.

[22] Sentry360. Fullsight IP 1.3 megapixel ultra-compact 360 degree dome. `http://sentry360.com/product/fs-ip-120/`.

[23] J. Volakis. *Antenna engineering handbook*. McGraw-Hill, 2007.

[24] C. Weidner. *NAST-M/K Horn Simulation*. Boulder Environmental Sciences and Technology, 2010. Analysis using QuickWave-V2D.

[25] I. Woodhouse. *Introduction to microwave remote sensing*. Taylor & Francis, 2006.